A hybrid-Trefftz finite element platform for solid and porous elastodynamics

Ionut Dragos Moldovan [a,*], Natàlia Climent [a], Elena Daniela Bendea [b], Ildi Cismasiu [c], António Gomes Correia [d]

[a] *CERIS, Instituto Superior Técnico, Universidade de Lisboa, Av. Rovisco Pais, 1049-001 Lisboa, Portugal*
[b] *Faculty of Civil Engineering, Technical University of Cluj-Napoca, Memorandumului 28, 400114 Cluj-Napoca, Romania*
[c] *UNIC, Faculdade de Ciências e Tecnologia, Universidade Nova de Lisboa, Monte de Caparica, Portugal*
[d] *ISISE, Escola de Engenharia, Universidade do Minho, Azurem, 4800-058 Guimarães, Portugal*

ARTICLE INFO

ABSTRACT

Hybrid-Trefftz finite elements are well suited for modeling the response of materials under highly transient loading. Their approximation bases are built using functions that satisfy exactly the differential equations governing the problem. This option embeds relevant physical information into the approximation basis and removes the well-known sensitivity of the conventional finite elements to high solution gradients and short wavelength excitations. Despite such advantages, no public software using hybrid-Trefftz finite elements to model wave propagation through solid and porous media exists to date. This paper covers the formulation and implementation of hybrid-Trefftz finite elements for single-phase, biphasic and triphasic media, subjected to dynamic loads. The formulation is cast in a unified framework, valid for the three types of materials alike, and independent of the nature (harmonic, periodic or transient) of the applied load. Displacement, traction, elastic and absorbing boundary conditions are accommodated. The implementation is made in three novel, open-source and user-friendly computational modules which are freely distributed online.

1. Introduction

Numerical models are essential to understand the behavior of materials under transient loading. However, in many cases, the high frequency content of transient excitations hinders the solution of dynamic problems with conventional (conforming) finite elements. Since conventional elements use simple, problem-independent approximation functions, at least ten (but preferably more) finite elements per wavelength are needed to correctly model the shape of the travelling waves. This restriction may be problematic even for single-phase (solid) materials, but it is particularly demanding when dealing with biphasic (saturated) and triphasic (unsaturated) porous materials. For such materials, secondary compression waves, of much shorter wavelengths than the primary compression waves, propagate through the fluid [9,18], and the pore-scale flow is an important source of dissipation. An additional difficulty posed to conventional finite elements is that, in many applications related with soil mechanics, the domain is semi-infinite, and special (and problem-dependent) boundary conditions need to be formulated on its far-field boundaries to avoid the reflection of the travelling waves back into the domain of interest. Calibration of the finite element size to the shortest wavelength relevant to the response of the medium, combined with the necessity of considering large subgrade areas to avoid spurious reflections from the fictitious boundary at far-field may lead to conventional finite element models that exceed the calculation capability of the average machine.

Hybrid-Trefftz finite elements can be used instead of conventional finite elements to mitigate these issues. The key feature of hybrid-Trefftz elements is that they use physically-meaningful approximation bases, specifically tailored for the problem that is being solved. Indeed, Trefftz-compliant approximation functions must satisfy exactly the differential equation governing the problem, meaning that the solution process is reduced to combining these functions to satisfy the boundary conditions in the best possible way. This option removes the restriction of using at least ten finite elements per wavelength and improves considerably the robustness of the results to mesh distortion and high solution gradients [17,20], supporting the use of large, high order finite elements for modeling transient problems.

The concept that stands at the base of the Trefftz methods was suggested by Trefftz [25] and the first application in the context of the finite element method was reported by Tong et al. [24]. Jirousek

---

[13] presented four hybrid-Trefftz formulations generally applicable to solid mechanics problems. Other significant contributions have been made after that by other authors, such as Herrera [11], Piltner [21], Qin [22] and Freitas et al. [9], among many others. In more recent studies, hybrid-Trefftz elements were developed for plates and shells [15], including particular solutions for cracking modes [10], and for the analysis of the eigenmodes of optical fibers [23]. Finally, Trefftz methods have also been combined with other methods, as for example with isogeometric analysis [12] for the solution of elastostatic problems.

Despite the advantages they offer over conventional elements, hybrid-Trefftz finite elements have only recently been included in public, user-friendly software. The computational platform FreeHyTE, presented at length in Moldovan and Cismaşiu [19], offers hybrid-Trefftz finite elements for the solution of a variety of elliptic, parabolic and hyperbolic boundary values problems, subjected to a considerable breadth of boundary conditions, and covering a wide range of physical problems. FreeHyTE is easy to use, as it features graphical user interfaces for the definition of the structure, as well as installation, user's and developer's manuals, and amenable to extension, as it includes a considerable breadth of standardized computational procedures and data structures usable with all Trefftz models, meaning that only formulation-specific coding needs to be performed. All FreeHyTE modules and their manuals are freely available for download under a GNU-GPL license [7].

Three new FreeHyTE modules are presented in this paper. The elements are designed for the solution of elastodynamic problems defined on solid (single-phase), saturated (biphasic) and unsaturated (triphasic) media.

The mathematical model used for saturated porous media is based on the Biot's theory [3]. For unsaturated porous media, the theory of mixtures with interfaces is adopted [26]. Both theories take into account the pore-scale fluid flow and are able to recover the secondary compression waves propagating through the fluids.

A unified formulation of hybrid-Trefftz finite elements valid for harmonic, periodic and transient problems defined on solid, saturated and unsaturated media is adopted. The original problem in time and space is discretized into a series of spectral problems in space after the expansion of the time variation of the involved fields into Daubechies wavelet series. For the solution of each spectral problem, the (generalized) displacement field is approximated in the domain of each finite element. The approximation basis is constrained to satisfy exactly the differential equation governing the problem (the Trefftz constraint). On the essential boundaries of the elements, tractions in the solid phase and pore pressures are independently approximated using bases subjected only to completeness and linear independence constraints (Chebyshev polynomials are used here). All approximations are constructed hierarchically and are not linked to the nodes of the elements.

Absorbing boundary conditions are formulated to enable the modeling of semi-infinite media. They are used to separate the domain of interest from the outer domain and designed to minimize the amount of energy reflected back into the domain of interest when a travelling wave hits the boundary. For solid and saturated materials, the absorbing boundary conditions reported in [14] and [9], respectively, are used. For unsaturated geomaterials, a novel absorbing boundary condition is proposed.

The formulation of the hybrid-Trefftz finite elements for elastodynamic problems is given in Section 2, followed by a description of their implementation in FreeHyTE in Section 3. In Section 4, three numerical examples involving solid, saturated and unsaturated materials subjected to shock loads are presented, and the results validated against results obtained with conventional finite elements and similar results found in the literature. Finally, the conclusions are given in Section 5.

2. Hybrid–Trefftz finite elements for elastodynamics

Hybrid–Trefftz finite elements feature physically meaningful approximation bases, built using functions that satisfy exactly all domain equa-
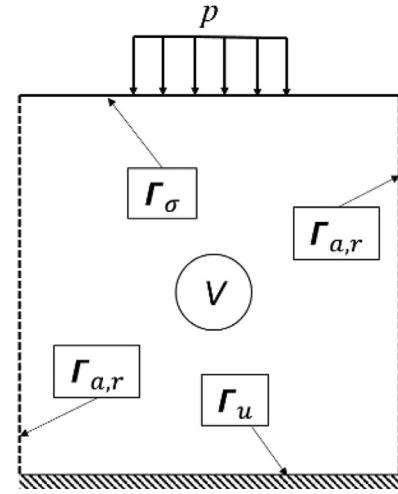

Fig. 1. Domain (V) with Dirichlet (Γ_u), Neumann (Γ_σ), absorbing (Γ_a) and Robin (Γ_r) boundaries.

tions (but not necessarily the boundary conditions). The weights of these functions are the main unknowns of the problem, as opposed to the nodal values of the approximated fields, as typical of the conventional finite elements. All bases are hierarchical, meaning that the redefinition of the nodes does not call for the redefinition of the approximation functions. Hybrid–Trefftz elements are less sensitive to issues like gross mesh distortion, nearly incompressible constituents, large solution gradients and very small wavelengths [20].

The general expressions of the elastodynamic equations are given in Section 2.1, followed by their time discretization in Section 2.2 and their adaptation to solid, saturated and unsaturated materials in Section 2.3. The formulation of hybrid-Trefftz elements for each of these cases is given in Section 2.4.

2.1. Governing elastodynamic equations

The elastodynamic problem is defined on a medium either made of a single (solid) phase, two phases (solid and wetting fluid), or three phases (solid, wetting fluid and non-wetting fluid). Regardless of the number of phases, the medium is considered (piecewise) homogeneous. It has a linear-elastic behavior, and displacements and deformations are considered small. Plane strain conditions are assumed for all types of materials. For solids, plane stress conditions are also included. Under these hypotheses, the elastodynamic equations in a domain V (Fig. 1) are written in the following general form:

$$D\sigma(x, y, t) = d_0\dot{u}(x, y, t) + \rho_0\ddot{u}(x, y, t) \tag{1}$$

$$\varepsilon(x, y, t) = D^*u(x, y, t) \tag{2}$$

$$\sigma(x, y, t) = k\varepsilon(x, y, t) \tag{3}$$

In the equilibrium Eq (1), body forces are neglected because their presence does not change the wave propagation patterns. Vector σ is the generalized stress vector, u is the generalized displacement vector, and matrices ρ_0 and d_0 collect the material density and dissipation components. Eq (2) is the compatibility condition, where ε is the generalized strain vector, and Eq (3) is the elasticity equation, where k is the material stiffness matrix. D and D^* are the (adjoint) differential equilibrium and compatibility operators, respectively.

The types of boundaries that can be defined on the domain V (Fig. 1) are: Dirichlet boundaries (Γ_u), where displacements are imposed, Neumann boundaries (Γ_σ), where tractions are imposed, absorbing boundaries (Γ_a), used to enforce a non-reflection criterion to simulate semi-

infinite domains [16], and Robin (elastic) boundaries (Γ_r), where a traction to displacement proportionality condition is enforced. The boundary conditions are described as,

$$\boldsymbol{u}(x, y, t) = \boldsymbol{u}_\Gamma(x, y, t) \quad (\text{on } \Gamma_u) \tag{4}$$

$$\boldsymbol{N}\boldsymbol{\sigma}(x, y, t) = \boldsymbol{t}_\Gamma(x, y, t) \quad (\text{on } \Gamma_\sigma) \tag{5}$$

$$\boldsymbol{u}(x, y, t) + \boldsymbol{C}\,\boldsymbol{t}(x, y, t) = 0 \quad (\text{on } \Gamma_a) \tag{6}$$

$$\boldsymbol{u}(x, y, t) + \boldsymbol{f}\,\boldsymbol{t}(x, y, t) = 0 \quad (\text{on } \Gamma_r) \tag{7}$$

where $\boldsymbol{t}_\Gamma$ and $\boldsymbol{u}_\Gamma$ represent the enforced boundary tractions and displacements, respectively, $\boldsymbol{t}$ are the boundary tractions, and matrix $\boldsymbol{N}$ collects the components of the outward normal to the Neumann boundary. Matrix $\boldsymbol{f}$ collects the flexibility coefficients in the normal and tangential directions to the Robin boundary and $\boldsymbol{C}$ is the flexibility matrix of the absorbing boundary.

It is assumed that the displacement field and its derivatives are null at $t = 0$. This assumption is true in a majority of practical wave propagation problems and supports important simplifications in the solution process. It is not, however, an intrinsic limitation of the Trefftz elements and formulations including non-null initial conditions were reported, for instance, in Moldovan et al. [18].

2.2. Discretization in time

The weighted residual algorithm suggested by Freitas [8] is applied to discretize Eqs (1)–(7) in time. All unknown fields are approximated independently over the total time of the analysis,

$$\boldsymbol{u}(x, y, t) = \sum_{n=1}^{N} W_n(t)\boldsymbol{u}_n(x, y) \tag{8}$$

$$\boldsymbol{\varepsilon}(x, y, t) = \sum_{n=1}^{N} W_n(t)\boldsymbol{\varepsilon}_n(x, y) \tag{9}$$

$$\boldsymbol{\sigma}(x, y, t) = \sum_{n=1}^{N} W_n(t)\boldsymbol{\sigma}_n(x, y) \tag{10}$$

$$\boldsymbol{t}(x, y, t) = \sum_{n=1}^{N} W_n(t)\boldsymbol{t}_n(x, y) \tag{11}$$

where $W_n(t)$ is the n-th term of the time basis and N designates its total number of functions.

Moreover, independent approximations are assumed for the velocity and acceleration fields,

$$\boldsymbol{v}(x, y, t) = \sum_{n=1}^{N} W_n(t)\boldsymbol{v}_n(x, y) \tag{12}$$

$$\boldsymbol{a}(x, y, t) = \sum_{n=1}^{N} W_n(t)\boldsymbol{a}_n(x, y) \tag{13}$$

The velocity and acceleration definitions $\dot{\boldsymbol{u}} = \boldsymbol{v}$ and $\dot{\boldsymbol{v}} = \boldsymbol{a}$ are enforced weakly using time basis functions W_m ($m = \{1, \dots, N\}$) for weighting, to yield,

$$\int_0^{\Delta t} \widehat{W_m}(\boldsymbol{v} - \dot{\boldsymbol{u}})dt = 0 \tag{14}$$

$$\int_0^{\Delta t} \widehat{W_m}(\boldsymbol{a} - \dot{\boldsymbol{v}})dt = 0 \tag{15}$$

where Δt is the total time and $\widehat{W_m}$ is the complex conjugate of W_m. Integrating by parts Eq (14) and taking into account that the initial conditions are assumed null, the following equation is obtained:

$$\int_0^{\Delta t} \widehat{W_m}\boldsymbol{v}dt = \widehat{W_m}(\Delta t)\boldsymbol{u}(\Delta t) - \int_0^{\Delta t} \widehat{W_m}\boldsymbol{u}dt \tag{16}$$

Substituting approximations (8) and (12) into Eq (16) and taking into account that generalized displacements $\boldsymbol{u}_n$ and velocities $\boldsymbol{v}_n$ are independent of time, one gets,

$$\Delta t \sum_{n=1}^{N} H_{mn}\boldsymbol{v}_n = \sum_{n=1}^{N} G_{mn}\boldsymbol{u}_n \tag{17}$$

where

$$H_{mn} = \frac{1}{\Delta t}\int_0^{\Delta t} \widehat{W_m}W_n dt \tag{18}$$

$$G_{mn} = \widehat{W_m}(\Delta t)W_n(\Delta t) - \int_0^{\Delta t} \widehat{W_m}W_n dt \tag{19}$$

In order to uncouple Eq (17), basis $\boldsymbol{W}(t)$ is constructed such that matrices $\boldsymbol{H}$ and $\boldsymbol{G}$ are proportional through a diagonal matrix $\boldsymbol{\Psi}$. This process, described in Moldovan [16], can be applied to any type of time basis and is thus not a limitation of this time integration procedure. Under these conditions, Eq (17) uncouples to yield,

$$\Delta t\boldsymbol{v}_n = \Psi_n\boldsymbol{u}_n \tag{20}$$

where Ψ_n is the n-th diagonal term of matrix $\boldsymbol{\Psi}$.

Applying a similar procedure to Eq (15) yields,

$$\Delta t\boldsymbol{a}_n = \Psi_n\boldsymbol{v}_n \tag{21}$$

Eqs (1) to (3) are enforced weakly in time, using basis $\boldsymbol{W}(t)$ for weighting. A series of N expressions is obtained for each equation:

$$\int_0^{\Delta t} \widehat{W_m}\big(\boldsymbol{D}\boldsymbol{\sigma} - \boldsymbol{d}_0\dot{\boldsymbol{u}} - \rho_0\ddot{\boldsymbol{u}}\big)dt = 0 \tag{22}$$

$$\int_0^{\Delta t} \widehat{W_m}\big(\boldsymbol{\varepsilon} - D^*\boldsymbol{u}\big)dt = 0 \tag{23}$$

$$\int_0^{\Delta t} \widehat{W_m}(\boldsymbol{\sigma} - \boldsymbol{k}\boldsymbol{\varepsilon})dt = 0 \tag{24}$$

Substituting Eqs (8),(10),(20) and (21) into Eq (22) and taking into account that matrices $\boldsymbol{H}$ and $\boldsymbol{G}$ are related through the diagonal matrix $\boldsymbol{\Psi}$, yield a set of N uncoupled problems of the following type:

$$\boldsymbol{D}\boldsymbol{\sigma}_n - \frac{\Psi_n^2}{\Delta t^2}\left(\rho_0 + \frac{\Delta t}{\Psi_n}\boldsymbol{d}_0\right)\boldsymbol{u}_n = 0 \tag{25}$$

Eq (25) can be written in the spectral form,

$$\boldsymbol{D}\boldsymbol{\sigma}_n + \omega_n^2\rho_n\boldsymbol{u}_n = 0 \tag{26}$$

where ω_n is a generalized frequency, defined as,

$$\omega_n = -i\frac{\Psi_n}{\Delta t} \tag{27}$$

where i is the imaginary unit, and

$$\rho_n = \rho_0 - \frac{i}{\omega_n}\boldsymbol{d}_0 \tag{28}$$

Finally, substituting Eqs (8) to (10) in Eqs (23) and (24), and applying the same procedure, one gets,

$$\boldsymbol{\varepsilon}_n = D^*\boldsymbol{u}_n \tag{29}$$

$$\boldsymbol{\sigma}_n = \boldsymbol{k}\boldsymbol{\varepsilon}_n \tag{30}$$

Eqs (26), (29) and (30) of each spectral problem can be collapsed into a single equation in V, the Navier equation,

$$D\left(kD^*u_n(x,y)\right) + \omega_n^2 \rho_n u_n(x,y) = 0 \tag{31}$$

In FreeHyTE, the time basis $W(t)$ is constructed using Daubechies wavelets [6]. Daubechies wavelets are consistent with the transient nature of the simulated phenomena and offer good accuracy even when large time steps are adopted for the analysis. Therefore, only one time step is used to model the whole duration of the problem. The number of time-discretized problems of type (31) is equal to the dimension of the time basis $W(t)$.

Similar discretization procedures are applied to boundary conditions (4) to (7), using approximations (8), (10) and (11), to yield,

$$u_n = u_{\Gamma_n} \text{ (on } \Gamma_u) \tag{32}$$

$$N\sigma_n = t_{\Gamma_n} \text{(on } \Gamma_\sigma) \tag{33}$$

$$u_{\Gamma_n} + Ct_{\Gamma_n} = 0 \text{ (on } \Gamma_a) \tag{34}$$

$$u_{\Gamma_n} + ft_{\Gamma_n} = 0 \text{ (on } \Gamma_r) \tag{35}$$

where,

$$u_{\Gamma_n} = \frac{1}{\Delta t} \sum_{m=1}^{N} \bar{H}_{nm} \int_0^{\Delta t} \widehat{W_m} u_\Gamma \, dt \tag{36}$$

$$t_{\Gamma_n} = \frac{1}{\Delta t} \sum_{m=1}^{N} \bar{H}_{nm} \int_0^{\Delta t} \widehat{W_m} t_\Gamma \, dt \tag{37}$$

and $\bar{H}_{nm}$ designates the generic term of the inverse of matrix H. The spectral problems defined by Eqs (26), and (29) to (35) are expressed in space variables only. Their solutions can be used to compute the time-dependent fields using approximations (8) to (10).

2.3. Elastodynamic models

Eqs (26) and (29) to (35) define the unified hybrid-Trefftz formulation, valid for solid, and saturated and unsaturated porous materials alike. However, the expressions of the terms present in these equations depend on the type of material and on the mathematical model, and are detailed below. To simplify notations, index n designating the n-th spectral problem is dropped from this point.

2.3.1. Single-phase media

The model adopted for single-phase media is based on the classical theory of elasticity. In Eqs (26) and (29) to (35), the stress vector $\sigma = \{\sigma_{xx} \ \sigma_{yy} \ \sigma_{xy}\}^T$ lists the normal and tangential stresses in the medium and the displacement vector $u = \{u_x \ u_y\}^T$ collects the displacement components in the Cartesian directions. The generalized mass matrix ρ depends on the material mass density. The stiffness matrix k depends on the type of plane state (plane stress or plane strain). The exact expressions of those matrices and differential operators D and D^* are given in Appendix A.

2.3.2. Biphasic media

The model adopted for biphasic (saturated) porous media is based on the Biot's theory [3]. In Biot's theory, the porous media is represented as an elastic solid phase fully permeated by a Darcy-compliant fluid phase. Both phases are assumed compressible. A solid displacement–fluid seepage (u-w) variant of Biot's theory is used to formulate the governing equations. The micro-scale fluid acceleration is included in the model. This option ensures that the model is able to capture the secondary compression wave propagating through the fluid motion in the micro-pores.

Eqs (26) and (29) to (35) can be used to describe the behavior of the biphasic material in accordance with the Biot's theory. The stress vector $\sigma = \{\sigma_{xx} \ \sigma_{yy} \ \sigma_{xy} \ \pi\}^T$ contains the components of the total stress tensor and the pore fluid pressure (π). The displacement vector $u = \{u_x \ u_y \ w_x \ w_y\}^T$ collects the displacement components in the solid phase $u^S = \{u_x \ u_y\}^T$ together with the fluid seepage components $w = \{w_x \ w_y\}^T$. The generalized mass matrix ρ depends on the mass density of the mixture, the mass density of the fluid phase, and the dissipation. The stiffness matrix k depends on the Lamé and Biot coefficients. The exact expressions of those matrices and differential operators D and D^* are given in Appendix B.

Finally, boundary condition (35) relates the normal and tangential components of the displacement and traction fields

$$\begin{pmatrix} u_n \\ u_t \\ w_n \end{pmatrix} + \begin{pmatrix} f_n & 0 & 0 \\ 0 & f_t & 0 \\ 0 & 0 & 0 \end{pmatrix} \begin{pmatrix} t_n \\ t_t \\ \pi \end{pmatrix} = 0 \tag{38}$$

where f_n and f_t are the flexibility coefficients of the elastic boundary in the normal and tangential directions. The last equation in the Robin boundary conditions (38) states that no seepage occurs, meaning that the elastic boundary is considered impervious.

2.3.3. Triphasic media

In triphasic (unsaturated) media, three immiscible phases are considered: the solid phase (S), the wetting fluid phase (W) and the non-wetting fluid phase (N) [4]. The mathematical model adopted for triphasic media is the theory of mixtures with interfaces suggested in Wei and Muraleetharan [26]. This theory includes the effect of the pore pressure gradients (macroscopic fluid flow) and neglects the effect of the capillary relaxation (microscopic fluid flow). The dynamic compatibility conditions on the micro-scale interfaces between the three phases are taken into account.

Eqs (26) and (29) to (35) also apply here. However, the vectors and matrices present in the governing equations have different components than for the biphasic case. The stress vector lists the components of the total stress tensor and the pore pressure in each of the two fluid phases, $\sigma = \{\sigma_{xx} \ \sigma_{yy} \ \sigma_{xy} \ \pi^W \ \pi^N\}^T$. The displacement vector collects the displacement components in the solid phase and in the fluid phases, $u = \{u_x^S \ u_y^S \ u_x^W \ u_y^W \ u_x^N \ u_y^N\}^T$. The remaining matrices and coefficients present in the governing equations for triphasic media are fully described in Appendix C.

Boundary condition (35) relates the normal and tangential components of the displacement and traction fields on a Robin boundary,

$$\begin{pmatrix} u_n \\ u_t \\ w_n^W \\ w_n^N \end{pmatrix} + \begin{pmatrix} f_n & 0 & 0 & 0 \\ 0 & f_t & 0 & 0 \\ f_n & 0 & 0 & 0 \\ f_n & 0 & 0 & 0 \end{pmatrix} \begin{pmatrix} t_n \\ t_t \\ \pi^W \\ \pi^N \end{pmatrix} = 0 \tag{39}$$

where f_n and f_t are the flexibility coefficients of the elastic boundary in the normal and tangential directions. Again, it should be noted that the Robin boundary conditions for the fluid phases are designed to enforce null boundary seepage in both fluids.

The absorbing boundary flexibility matrices present in Eq (34) are described for solid, biphasic and triphasic media in Appendix D.

2.4. Hybrid–Trefftz finite element model

2.4.1. Approximations of displacements and tractions

Eq (31) is solved using the displacement model of the hybrid-Trefftz finite element formulation.

Let the domain V presented in Fig. 1 be divided into finite elements V^e (Fig. 2) and let the interior boundaries (Γ_i^e) be defined as the boundaries of the element that are not exterior boundaries of the domain.

The (generalized) displacement field u is approximated in each finite element V^e as,

$$u = U X \tag{40}$$

where matrix U collects Trefftz-compliant approximation functions, meaning that the functions included in basis U are bounded to satisfy
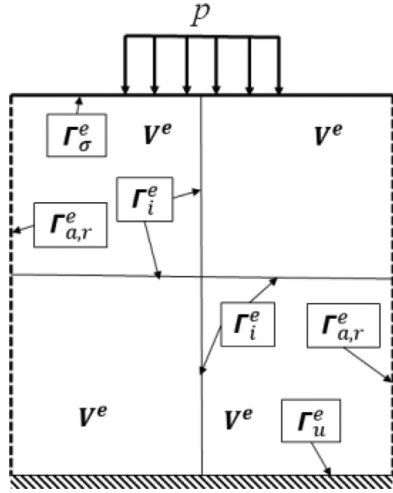
Fig. 2. Finite elements, Neumann, Dirichlet, Robin, absorbing and interior boundaries.

exactly the Navier Eq (31). Their explicit expressions for each type of medium are derived in Section 2.4.3.

The tractions in the solid phase and the pore pressures are approximated independently on the essential boundary $\Gamma_e^e = \Gamma_u^e \ U \ \Gamma_a^e \ U \ \Gamma_r^e \ U \ \Gamma_i^e$ of the element as,

$$t = Zp \tag{41}$$

Bases U and Z are independent of each other, constructed strictly hierarchically, and not linked to the nodes of the elements, and X and p are the weights of the approximation functions, with no particular physical meaning.

2.4.2. Explicit form of the Navier equation

Single-phase media. The definitions of the mass and stiffness coefficients listed in Appendix A are inserted into the Navier Eq (31), to yield,

$$\nabla\left[\left(k_{12} + k_{33}\right)\nabla^T u\right] + k_{33}\nabla^2 u + \omega^2 \rho u = 0 \tag{42}$$

where k_{12} and k_{33} are coefficients of the stiffness matrix k, ρ is the (diagonal) coefficient of the mass matrix ρ, ∇ is the gradient operator and ∇^2 is the Laplacian operator.

Biphasic media. Substituting the definitions given in Appendix B into the Navier Eq (31), two coupled differential equations are generated for biphasic media [16]

$$\nabla\left[\left(k_{12} + k_{33}\right)\nabla^T u^S + k_{14}\nabla^T w\right] + k_{33}\nabla^2 u^S + \omega^2\left(\rho u^S + \rho_w w\right) = 0 \tag{43}$$

$$\nabla\left[k_{14}\nabla^T u^S + k_{44}\nabla^T w\right] + \omega^2\left(\rho_w u^S + \rho_{w2} w\right) = 0 \tag{44}$$

where k_{12}, k_{33}, k_{14} and k_{44} are coefficients of the stiffness matrix k, and ρ, ρ_w and ρ_{w2} are coefficients of the mass matrix ρ.

Triphasic media. For triphasic media, substituting the definitions given in Appendix C into the Navier Eq (31), three coupled differential equations are obtained [5],

$$\nabla\nabla^T\left[\left(M_{SS} + n^S\mu^S\right)u^S + M_{SW}u^W + M_{SN}u^N\right] + n^S\mu^S\nabla^2 u^S + \omega^2\left(\rho_{SS}u^S + \rho_{SW}u^W + \rho_{SN}u^N\right) = 0 \tag{45}$$

$$\nabla\nabla^T\left[M_{SW}u^S + M_{WW}u^W + M_{WN}u^N\right] + \omega^2\left(\rho_{SW}u^S + \rho_{WW}u^W\right) = 0 \tag{46}$$

$$\nabla\nabla^T\left[M_{SN}u^S + M_{WN}u^W + M_{NN}u^N\right] + \omega^2\left(\rho_{SN}u^S + \rho_{NN}u^N\right) = 0 \tag{47}$$

2.4.3. Trefftz-compliant approximation functions

The functions to be included in the displacement approximation bases U for each type of medium must be selected from the solution space of the Navier problems derived in the previous section.

According to the Helmholtz principle, the generalized displacement fields can be written as the sum of the irrotational and solenoidal components of some displacement potentials ϕ, to yield,

$$u = \nabla\phi_P^S + \tilde{\nabla}\phi_S^S \quad \text{(for single − phase media)} \tag{48}$$

$$u^S = \nabla\phi_P^S + \tilde{\nabla}\phi_S^S \quad \text{(for biphasic and triphasic media)} \tag{49}$$

$$w = \nabla\phi_P^W + \tilde{\nabla}\phi_S^W \quad \text{(for biphasic media)} \tag{50}$$

$$u^{W,N} = \nabla\phi_P^{W,N} + \tilde{\nabla}\phi_S^{W,N} \quad \text{(for triphasic media)} \tag{51}$$

where $\tilde{\nabla}$ is the curl operator and superindices {S, W, N} correspond to the solid phase S, the fluid phase W in biphasic media, and the two fluid phases W and N in the triphasic media, and subindices {S, P} correspond to the shear and compression waves, respectively.

The Helmholtz decomposition (48) to (51) uncouples Navier equations into an irrotational motion described by potentials $\phi_P^{S,W,N}$, and a shear (solenoidal) motion, described by potentials $\phi_S^{S,W,N}$. Therefore, Navier equations are reduced to a set of uncoupled Helmholtz equations, of type,

$$\nabla^2\phi_{S,P_i}^{S,W,N} + \beta_{S,P_i}^2\phi_{S,P_i}^{S,W,N} = 0 \tag{52}$$

Wave numbers β_{S,P_i} (defined below) depend on the spectral frequency ω and material characteristics, and $i = 1$ for single-phase media, $i = \{1, 2\}$ for biphasic media and $i = \{1, 2, 3\}$ for triphasic media. This means that, in single-phase materials, a single compression wave and a single shear wave are identified for a given frequency value. In biphasic media, the potential functions $\phi_{S,P_i}^{S,W}$ define two compression waves (*P1* and *P2*) and one shear wave (*S*), and in triphasic media $\phi_{S,P_i}^{S,WN}$ define three compression waves (*P1, P2* and *P3*) and one shear wave (*S*).

The solutions of the Helmholtz Eq (52) in two dimensions using a polar referential (r, θ), are of type

$$\phi_{S,P_i}^{S,W,N}(r,\theta) = J_k\left(\beta_{S,P_i}r\right)\exp\left(i\,k\theta\right) \tag{53}$$

where $J_k(\beta r)$ is the Bessel function of the first kind and integer order k.

The trademark feature of the Trefftz elements is that the approximation functions included in basis U are chosen such as to satisfy exactly the Navier equation governing the problem. They are generated from the compression and shear potentials using the Helmholtz decomposition principle:

$$U_{P_i}^S = \nabla\phi_{P_i} \tag{54}$$

$$U_S^S = \tilde{\nabla}\phi_S \tag{55}$$

$$U_{P_i}^{W,N} = \gamma_{P_i}^{W,N}\nabla\phi_{P_i} \tag{56}$$

$$U_S^{W,N} = \gamma_S^{W,N}\tilde{\nabla}\phi_S \tag{57}$$

where $U_{P_i}^S$ lists the approximation functions of the displacements of the solid phase for the compression (P_i) waves; U_S^S are the approximation functions of the displacements of the solid phase for the shear (S) wave; $U_{P_i}^{W,N}$ corresponds to the displacements of the fluids for the compression (P_i) waves; and $U_S^{W,N}$ corresponds to the displacements of the fluids for the shear wave.

Single-phase media. In single-phase media, the wave numbers are defined by

$$\beta_S^2 = \frac{\rho}{k_{33}}\omega^2 \tag{58}$$

$$\beta_P^2 = \frac{\rho}{k_{12}+2k_{33}}\omega^2 \tag{59}$$

Biphasic media. The shear wave multiplier γ_S^W for biphasic media is

$$\gamma_S^W = -\frac{\rho_w}{\rho_{w2}} \tag{60}$$

and the compression wave multipliers $\gamma_{P_i}^W$ for biphasic media are the solutions of the equation

$$\left(1-\alpha\frac{\rho_{w2}}{\rho_w}\right)\left(\gamma_{P_i}^W\right)^2 + \left(\frac{\rho}{\rho_w}-\chi\frac{\rho_{w2}}{\rho_w}\right)\gamma_{P_i}^W + \left(\alpha\frac{\rho}{\rho_w}-\chi\right)=0 \tag{61}$$

where,

$$\chi = \alpha^2 + \frac{\lambda+2\mu}{M} \tag{62}$$

The wave numbers for biphasic media are

$$\beta_S^2 = \left(1+\gamma_S^W\frac{\rho_w}{\rho}\right)\frac{\rho}{\mu}\omega^2 \tag{63}$$

$$\beta_{P_i}^2 = \frac{\rho_w+\gamma_{P_i}^W\rho_{w2}}{\left(\alpha+\gamma_{P_i}^W\right)M}\omega^2 \tag{64}$$

All mechanical parameters used in the definitions above are defined in Appendix B.

Trihasic media. For triphasic media, a similar process is used to obtain the wave multipliers and wave numbers. For the shear wave, they are

$$\gamma_S^W = -\frac{\rho_{SW}}{\rho_{WW}} \tag{65}$$

$$\gamma_S^N = -\frac{\rho_{SN}}{\rho_{NN}} \tag{66}$$

$$\beta_S^2 = \frac{\rho_{SS}+\gamma_S^W\rho_{SW}+\gamma_S^N\rho_{SN}}{n^S\mu^S}\omega^2 \tag{67}$$

For the compression waves, the wave multipliers and wave numbers are the solutions of the eigenproblem

$$\left[-\frac{\beta_{P_i}^2}{\omega^2}\begin{pmatrix} M_{SS}+n^S\mu^S & M_{SW} & M_{SN} \\ M_{SW} & M_{WW} & M_{WN} \\ M_{SN} & M_{WN} & M_{NN} \end{pmatrix} + \begin{pmatrix} \rho_{SS} & \rho_{SW} & \rho_{SN} \\ \rho_{SW} & \rho_{WW} & 0 \\ \rho_{SN} & 0 & \rho_{NN} \end{pmatrix}\right]$$
$$\times \begin{pmatrix} \gamma_{P_i}^S \\ \gamma_{P_i}^W \\ \gamma_{P_i}^N \end{pmatrix} = \begin{pmatrix} 0 \\ 0 \\ 0 \end{pmatrix} \tag{68}$$

All mechanical parameters used in definitions (65) to (68) are defined in Appendix C.

2.4.4. Hybrid-Trefftz finite element formulation

Enforcing weakly Eq (31) in the domain of the element, Eq (32) on its Dirichlet (and interior) boundaries, Eq (34) on its absorbing boundaries, and Eq (35) on its Robin boundaries, yields,

$$\int \hat{U}^T\left(D\left(kD^*u\right)+\omega^2\rho u\right)dV^e = 0 \tag{69}$$

$$\int \hat{Z}^T\left(u-u_\Gamma\right)d\Gamma_{u,i}^e = 0 \tag{70}$$

$$\int \hat{Z}^T\left(u+Ct_\Gamma\right)d\Gamma_a^e = 0 \tag{71}$$

$$\int \hat{Z}^T\left(u+ft_\Gamma\right)d\Gamma_r^e = 0 \tag{72}$$

where $\hat{U}^T$ and $\hat{Z}^T$ are the transposed conjugates of bases U and Z. Finally, integrating by parts Eq (69) and substituting approximations (40) and (41), the problem is reduced to solving the algebraic system [9,16]

$$\begin{pmatrix} D & -B_{a/r} & -B \\ -\hat{B}_{a/r}^T & D_a/D_r & 0 \\ -\hat{B}^T & 0 & 0 \end{pmatrix}\begin{pmatrix} X \\ p_{a/r} \\ p \end{pmatrix} = \begin{pmatrix} f_t \\ 0 \\ -q_u \end{pmatrix} \tag{73}$$

where,

$$D = \int \hat{U}^T N S d\Gamma^e \tag{74}$$

$$D_a = -\int Z^T C Z d\Gamma_a^e \tag{75}$$

$$D_r = -\int Z^T f Z d\Gamma_r^e \tag{76}$$

$$B = \int \hat{U}^T Z d\Gamma_{u,a,r}^e \tag{77}$$

$$f_t = \int \hat{U}^T t_\Gamma d\Gamma_\sigma^e \tag{78}$$

$$q_u = \int \hat{Z}^T u_\Gamma d\Gamma_{u,i}^e \tag{79}$$

Neumann boundary conditions (33) are explicitly enforced in the boundary terms that emerge from the integration by parts of Eq. (69). Compliance of basis U with the Trefftz condition causes all domain integrals to vanish from the calculation.

Unlike the governing systems of conventional finite elements, system (73) is not always kinematically indeterminate. The system is called *kinematically indeterminate* if the kinematic variables collected in vector X cannot be determined strictly from the second set of equations. To ensure that no dependencies occur in the solving system (73), the kinematic indeterminacy conditions must be satisfied through an adequate truncation of approximation bases U and Z in the finite elements and on their boundaries, respectively. Namely, the system is kinematically indeterminate if the total number of approximation functions collected in the traction bases on the Dirichlet and interior boundaries is inferior to the total number of approximation functions collected in the domain bases. Robin and absorbing boundary bases are neutral to the kinematic indeterminacy condition.

3. FreeHyTE modules for elastodynamic problems

In this section, the FreeHyTE modules for the solution of elastodynamic problems in two dimensions are introduced. They are the *Solid Transient* module for problems involving single-phase media, *Biphasic Transient* module for problems defined on saturated porous media and the *Triphasic Transient* module, for problems involving unsaturated porous media.
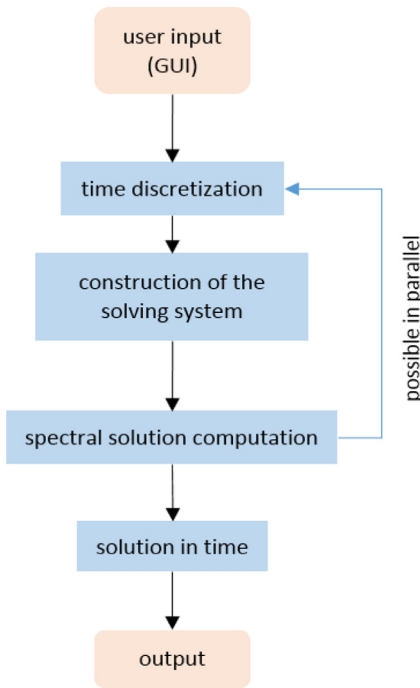
Fig. 3. Structure of the FreeHyTE modules.

3.1. Computational architecture

The general structure of a FreeHyTE module is described in Fig. 3. The user input is the first step and consists of a sequence of graphical user interfaces (GUIs) where the problem and the solution parameters are defined. These interfaces are presented and explained in Section 3.2. After this phase, FreeHyTE performs the time discretization (see Section 2.2), reducing the original problem in time and space to a

series of spectral problems in space and generates the input data for each of those problems. Each spectral problem is independent of the others, supporting a simple parallel solution process.

In the next step, each spectral problem is solved and the resulting spectral displacement fields are computed according to approximation (40). The stress and pore pressure fields are computed by enforcing the compatibility and elasticity equations on the displacement approximation,

$$\sigma = \mathcal{D}\left(kD^*U\right)X \qquad (80)$$

The integrations required for the computation of the coefficients of the solving systems (73) are performed numerically using the Gauss–Legendre quadrature rule. While accountable for the super convergence of the Trefftz finite elements, the physically meaningful approximation functions can hinder the numerical stability of the solution procedure, especially when the wave numbers associated to the compression waves propagating through the different phases are multiple orders of magnitude different from one another. To mitigate such issues, scaling, preconditioning and special system solvers are employed. They are described in more depth in Section 3.3.

When all spectral problems have been solved, the solution in time is calculated as a linear combination of the spectral solutions with the time basis, according to definitions (8) to (10). The time basis is constructed using Daubechies wavelets, which offer good accuracy even with very large time steps. The solutions in time can be plotted and/or saved in output files, as shown in Section 3.4.

3.2. Graphical user interfaces

The FreeHyTE GUI consists of four main interfaces, complemented by the Matlab's *pdetool* interface for the definition of non-regular domains and meshes. Their presentation is illustrated with the GUIs of the Triphasic Transient module. The GUIs of the other two modules are just simplified versions of those in Triphasic Transient.

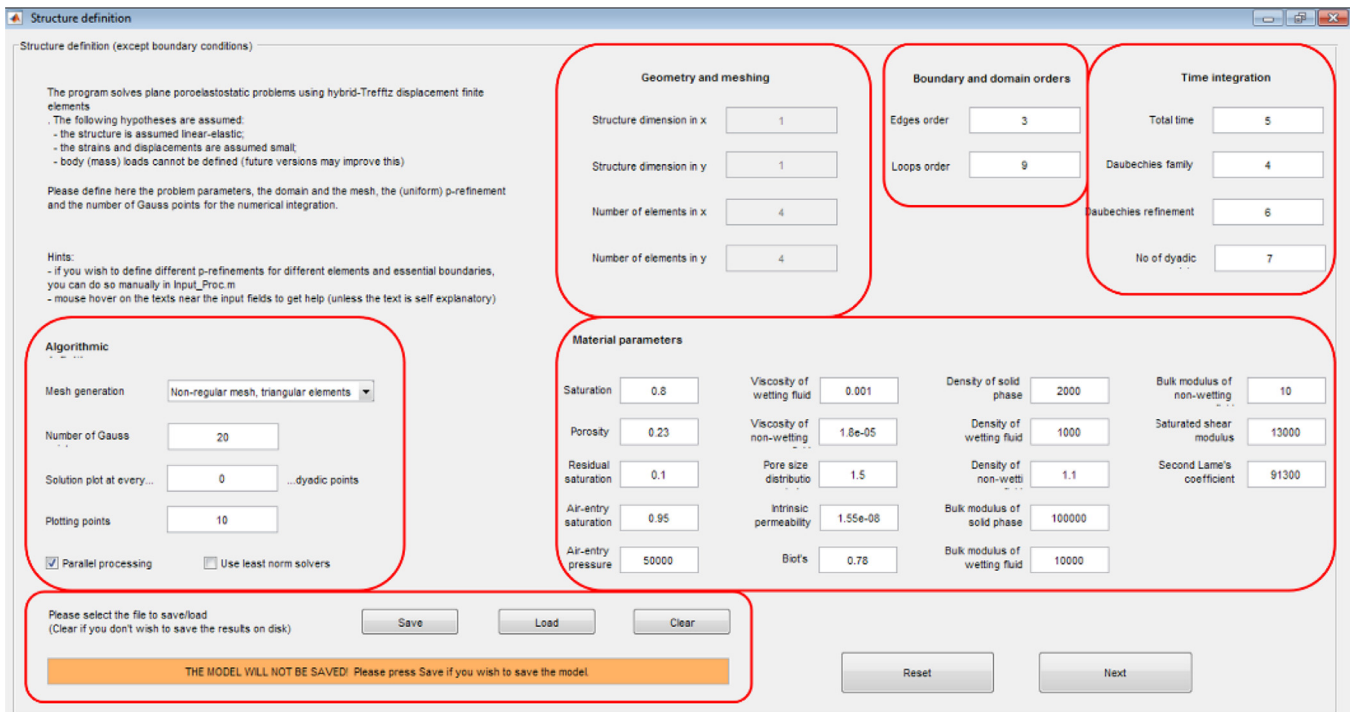Fig. 4 presents the first GUI. The main data zones of the interface are identified with red frames.
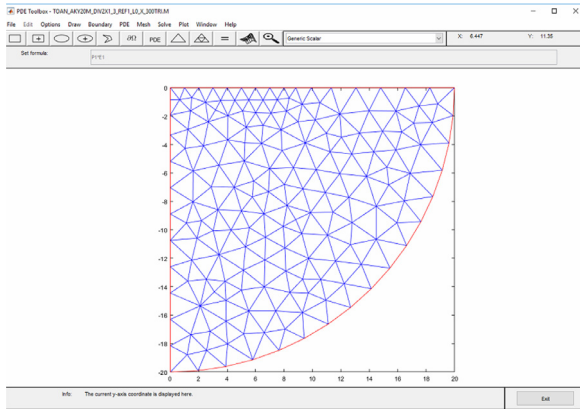

Fig. 4. Layout of GUI 1.

Fig. 5. Matlab's *pdetool* interface.

At the bottom of the first GUI are the '*Load*' and '*Save*' buttons: with the '*Load*' button the user can load previously saved problems and with the '*Save*' button the user can save the data of the current problem in a *.mat file. When the model is saved, FreeHyTE also stores the output data in output files.

The '*Algorithmic definitions*' zone is where the user must choose between the two automatic mesh generators built in FreeHyTE. The regular mesh generator creates meshes of uniform rectangular elements and should be used to discretize rectangular domains. The non-regular mesh generator creates triangular elements and can be used for any geometry. Additionally, the user must specify the number of Gauss-Legendre quadrature points and the number of plotting points where the solution is stored in the output files. Two important algorithmic options correspond to checkboxes '*Parallel processing*', which enables and disables the parallel solution of the time-discretized problems, and '*Use least norm solvers*', which enables FreeHyTE to use least norm solvers on ill-conditioned solving systems. Finally, the user can request the solutions to be plotted at a certain number of equally spaced (dyadic) time steps.

In '*Geometry and meshing*', the user can define a regular structure and mesh. This zone is only editable when a regular mesh is chosen. In the '*Boundary and domain orders*' zone, the user can set the orders of approximations in the domain of the elements (*Loops order*) and on their essential boundaries (*Edges order*). *Loops order* corresponds to the order of the Bessel functions in Eq (53) and *Edges order* corresponds to the order of the Chebyshev polynomials used for the construction of traction basis $\mathbf{Z}$ on the essential boundaries (Eq (41)).

The material parameters required for the execution of the analysis are set in '*Material parameters*'. In the '*Time integration*' zone, the user specifies the total time of the analysis and the three calibration parameters that control the Daubechies wavelet basis. Daubechies wavelets are functions with no analytic expression, meaning that their values can only be computed in certain, equally spaced points on their support, called dyadic points. The total time of the simulation is divided into 2^d time intervals, to which correspond $2^d + 1$ dyadic points, where d is set in the '*No of dyadic points*' field of the interface (Fig. 4). Therefore, each time interval is $\frac{T}{2^d+1}$, where T is the total time of the simulation. The wavelet family number represents the number of vanishing moments of the wavelet, and the order (p) of the time basis controls the number of functions that are included in the basis, which is equal to 2^p. It is noted, however, that only 2^{p-1} spectral runs are required to compute the solution, as spectral analyses yield pairs of complex conjugate solutions.

When the non-regular mesh generator is chosen, Matlab's *pdetool* interface is launched in the next step (Fig. 5). In this interface, the domain can be created by addition or substraction of simple geometrical shapes and meshed using triangular finite elements. The maximum leading dimension of the elements and the growth rate of the mesh are parameters defined by the user.

The second GUI (Fig. 6) is used to define the type of boundary (Dirichlet, Neumann, Robin or absorbing) for each exterior side of the domain. The structure visualization zone is located on the left side of GUI 2. It consists of a plot of the mesh, with buttons to display the structure information (nodes, edges or elements). The '*Enlarge*' button at the bottom can be used to open a separate interface to easily read the structural data in case the visualization area in GUI 2 is too small. The external boundaries of the structure are listed in the central zone of GUI 2 and the boundary types can be assigned in the right side of the interface.

The third GUI is presented in Fig. 7. The three input areas are used to define the Dirichlet, Neumann and Robin boundary conditions. Absorbing boundary conditions require no input from the user, as FreeHyTE automatically computes the flexibility coefficients. The definition of the space variations of the boundary displacement and traction fields is made by specifying their values in as many equally spaced points along the boundary as needed to define a polynomial variation. The time variation of the fields can be defined by any expression in the time variable t that can be evaluated by Matlab. The definition of the Robin boundary conditions only requires the input of the flexibility coefficients in the normal and tangential directions.

Finally, the last step before launching the execution of FreeHyTE is the verification GUI (Fig. 8). This GUI is meant to allow the user to verify the definitions of the structure and boundary conditions by selecting the
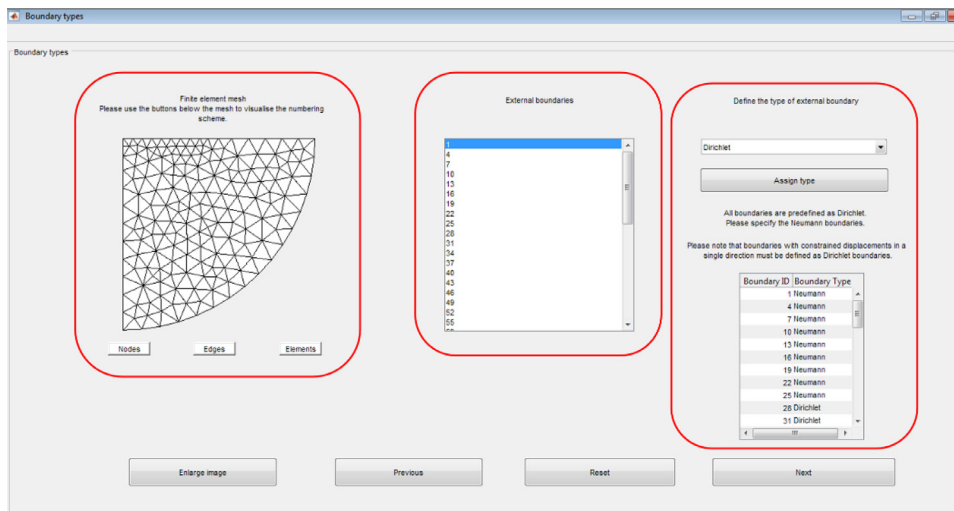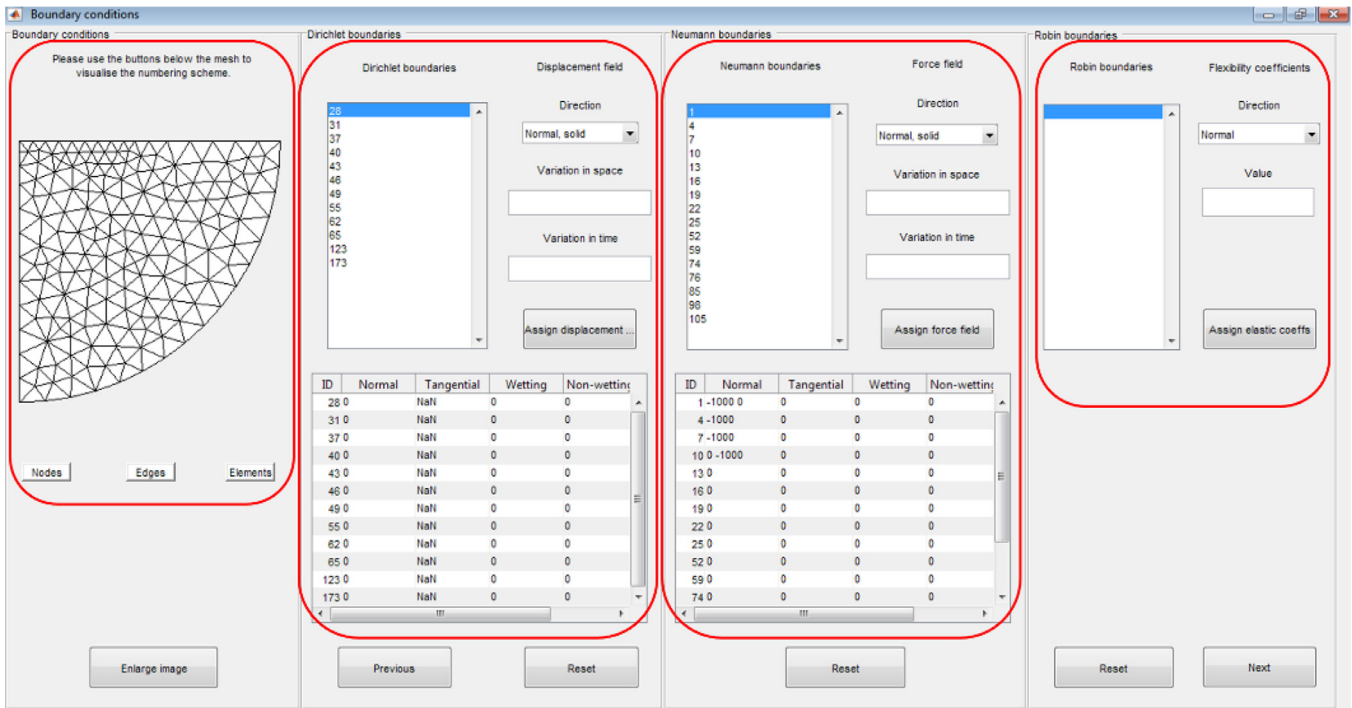

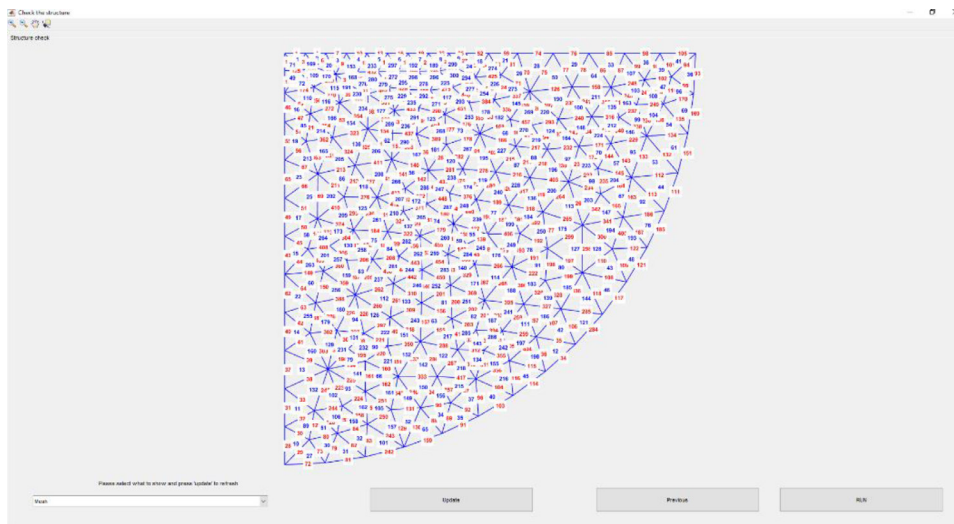**Fig. 6.** Layout of GUI 2.

Fig. 7. Layout of GUI 3.

Fig. 8. Layout of GUI 4.

desired visualization in the pop-up menu on the left side. For example, the visualization interface for the boundary conditions in the normal direction is shown in Fig. 9, where Dirichlet sides are plotted in black, Neumann sides are plotted in red and absorbing sides are plotted in green. The nodal values of the boundary conditions are listed on each boundary.

3.3. Processing

During the execution, the solution of each spectral problem can be parallelized. In the parallel processing mode, the default option is to summon all cores of the machine to perform the calculations. However, the number of cores can be controlled by editing a field in the code. Large analyses should be run in parallel as it significantly decreases the computational time. The parallel processing mode requires Matlab's Parallel Computing Toolbox. If it is not available, FreeHyTE will run se-

quentially regardless of whether the '*Parallel processing*' option (Fig. 4) is turned on or off.

In order to improve the numerical stability of the calculations, the convergence rates and the condition number of the solving system, scaling procedures are applied to the input parameters, approximation functions and solving system.

The scaling of the input parameters consists of the scaling of the original material and geometrical quantities. Let a generic quantity x be scaled such that,

$$x = x_S \cdot \bar{x} \tag{81}$$

where x_S is the scaling factor and $\bar{x}$ is the scaled version of x. Primary scaling factors are set for the material moduli (E_S), densities (ρ_S), lengths and coordinates (L_S) and tractions and stresses (t_S). They are defined as the maximum values of the respective quantities taken over all elements of the mesh. Three secondary scaling factors for the spectral frequency,
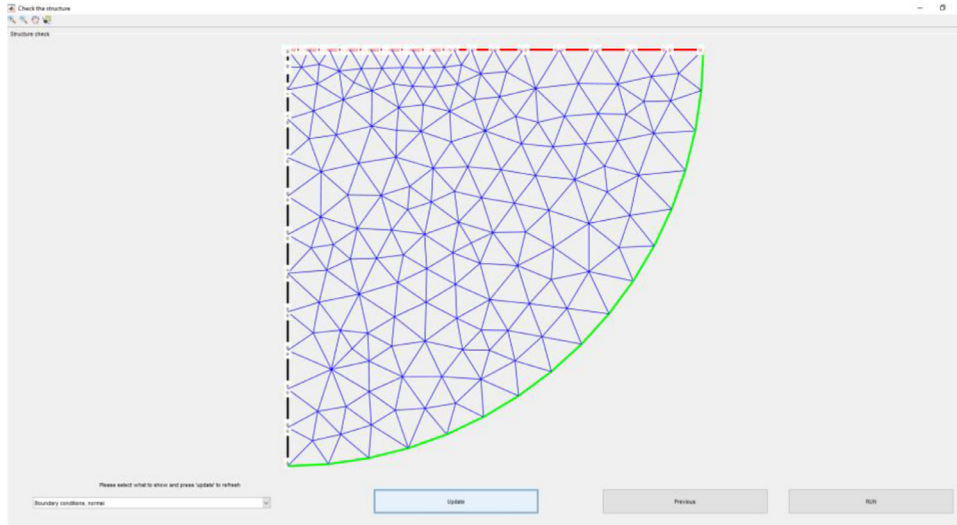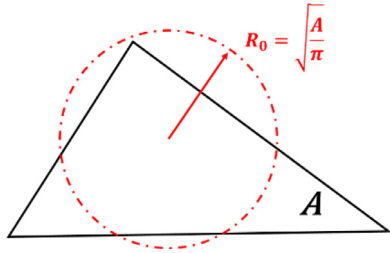
Fig. 10. Finite element with area A and the circumference with the same area and radius R_0.

displacements and flexibility coefficients of the elastic boundaries are derived such as to preserve the form of all governing equations. They are defined as, respectively,

$$\omega_S = \sqrt{\frac{E_S}{\rho_S \cdot L_S^2}} \tag{82}$$

$$u_S = \frac{t_S \cdot L_S}{E_S} \tag{83}$$

$$f_S = \frac{L_S}{E_S} \tag{84}$$

The approximation function scaling consists in the scaling of the shape functions U by dividing them by $|J_k(\beta_{S,P_i} R_0)|$, where $R_0 = \sqrt{\frac{A}{\pi}}$ is the radius of the circumference with the same area (A) as the finite element (Fig. 10).

Another technique FreeHyTE uses to improve the numerical stability is the preconditioning of the solving system. The procedure equilibrates the values of the diagonal terms of system (73), bringing their modules close to unity. Considering a generic linear system $Ax = b$, where A is a square, possibly Hermitian, matrix and x and b are vectors, then, the system may be written in the scaled form,

$$\bar{A}\bar{x} = \bar{b} \tag{85}$$

where the scaled arrays are defined as,

$$\bar{A} = \hat{S}^T A S \tag{86}$$

$$\bar{x} = S^{-1} x \tag{87}$$

$$\bar{b} = \hat{S}^T b \tag{88}$$

and S represents a diagonal scaling matrix, whose terms are defined as the square roots of the diagonal terms of the matrix A. When a null diagonal term is encountered in matrix A, the respective scaling term is equal to one, meaning that no scaling is applied to the respective lines and columns. This scaling procedure preserves the symmetry of the original system.

Finally, when the system is ill-conditioned and the '*Use least norm solvers*' checkbox is enabled (Fig. 4), FreeHyTE uses least norm solvers for the solution of system (73). Matlab's least norm solver attempts to find the solution that minimizes the error norm of the solving system using an iterative procedure. The solution is based on the computation of the Moore-Penrose pseudoinverse of the matrix. The procedure's convergence threshold and the maximum number of iterations can be controlled by advanced users by modifying a line in the code. The convergence to a strong solution using the iterative least norm solver can be extremely slow. Refining the mesh and reducing the orders of the domain and boundary bases is the best way to avoid ill-conditioned systems.

3.4. Outputs

The (generalized) displacement and stress fields are stored in output files when the problem is saved. The solutions are computed in all $2^d + 1$ dyadic points and stored in separate *.dat files. The values of the fields are calculated in PP^2 plotting points in each finite element, where PP is the plotting points number input by the user in the first GUI (Fig. 4). The output files are formated for direct loading in the post-processing software Tecplot, but can be used with other visualization software as well as, for example, Paraview.

FreeHyTE also can produce plots of the solutions using Matlab's native plotting functions. Color map plots of the displacements, seepage, stresses and pore pressure fields are rendered. The plots are made at every NDP dyadic points, where the NDP parameter is controlled by user by editing the '*Solution plot at every… dyadic points*' box in the first GUI (Fig. 4). If a zero is set in this box this output, no color map plots are produced. It is noted that Matlab's native plotting functions can be tediously slow, so the solution plotting in specialized post-processing software is recommended.

4. Numerical examples

Three simulations are performed with the new FreeHyTE modules, aimed at illustrating the potential of hybrid-Trefftz finite elements to model highly transient wave propagation through bounded and unbounded media. The first simulation, presented in Section 4.1, is a
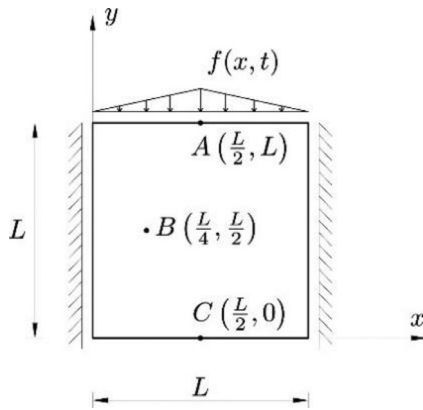
Fig. 11. Physical model of the simulation of a shock wave in a solid medium.

Table 1
Mechanical properties of the solid medium.

Density ρ (kg/m^3)	1000
Young's modulus E (Pa)	$1.00 \cdot 10^4$
Poisson's coefficient v	0.1

shock wave propagation in a bounded and an unbounded solid media, under plane strain conditions. To validate the FreeHyTE results, the bounded problem is solved using the conventional finite element software Abaqus. In Section 4.2, a simulation of the propagation of a shock wave through a semi-infinite saturated porous medium is presented. The results obtained with FreeHyTE are compared with those reported by Akiyoshi et al. [1] who solved a similar problem. The third simulation reproduces a similar excitation in an unbounded unsaturated medium and is discussed in Section 4.3.

4.1. Shock wave propagation in a solid medium

The first numerical example involves the propagation of a shock wave through a bounded and a (semi-) unbounded continua. The results obtained on the bounded medium are compared with those of the commercial finite element platform Abaqus. The results obtained on the unbounded medium are compared to those obtained with a fixed boundary to assess the presence of spurious reflections from the absorbing boundary.

The physical model is presented in Fig. 11. The medium is contained by frictionless lateral boundaries, under plane strain conditions. The bottom boundary of the medium is either rigid and frictionless (in the bounded case), or defined as an absorbing boundary (in semi-unbounded case). The shock vertical load is applied on the $L = 1.5$ m boundary at the top of the medium. Its amplitude is null on the sides of the medium, equal to 1 kPa in its middle and has a linear variation in space. In time, the applied load is constant in the first 0.05 s of the total duration of the analysis $T = 1.4$ s and null for $0.05 \ s < t \leq T$. The material properties are described in Table 1.

The medium is discretized in space using a regular mesh of 144 hybrid-Trefftz finite elements of size $\frac{L}{12}$. The orders of the domain and boundary bases are defined as 17 and 8, respectively. The total number of degrees of freedom (that is, the total dimension of the solving system (73)) is 15,156. The time discretization is performed using a Daubechies basis with scaling functions of family 4 and order 7. This generates 128 pseudo-spectral problems in space of type (31)–(35). Since they come in pairs of complex conjugates, however, only 64 problems actually need to be solved.

To validate the results obtained with FreeHyTE, the same problem is solved using the commercial software Abaqus, using 8-node (quadratic) conforming finite elements. The mesh consists of 112,500 finite elements, for a total of 252,472 degrees of freedom. The time discretiza-

tion is performed using the HHT time stepping scheme and time steps of 0.011 s.

The time-histories of the vertical displacement at point A (Fig. 11) and horizontal displacement at point B obtained with Abaqus (solid line) and FreeHyTE (dashed line) are presented in Fig. 12.

The application of the load causes a sudden increase in the magnitude of the vertical displacements in point A. After the load is withdrawn, the displacements remain with negative values until the wave front, reflected from the bottom boundary, returns at the top (just before 1s), when the vertical displacement changes sign. In point B, the horizontal displacements are null until the wave front arrives. The intensity of the lateral displacements in B is roughly one order of magnitude inferior to that of the vertical displacements in point A and the pattern less regular. Very good agreement is observed between the FreeHyTE and Abaqus results at all times.

The time-histories of the normal stresses in the vertical direction at points A and C (Fig. 11) and of the shear stress at point B obtained with Abaqus (solid line) and FreeHyTE (dashed line) are presented in Fig. 13. Standard stress smoothing/averaging is used in Abaqus. The numerical procedure used in FreeHyTE lacks numerical damping [16], so a basic FIR low-pass filter is used in post-processing.

The solutions obtained with Abaqus and FreeHyTE are quite similar in all plots, despite the vast difference in the number of degrees of freedom of the models. Some spurious vibrations of the solution exist in both solutions at point A (Fig. 13(a)) and, in the FreeHyTE solution, in point C (Fig. 13(c)). The Abaqus solution predicts a spurious vertical stress oscillation at point A (Fig. 13(a)) around the time of the arrival of the rebound of the shock wave, which is (correctly) not present in the FreeHyTE solution. Indeed, since the vertical load applied to the surface of the medium is null after the first 0.05 s, the vertical stresses on the free surface of the medium should be exactly zero after that. A detail of the vertical stress field on the upper 0.65m of the medium in the moment when this happens (0.95 s) is given in Fig. 14. It can be seen that a spurious bulb of vertical stress, albeit of low intensity, pollutes the Abaqus solution in the central region of the free surface.

For a more general perspective of the solutions, the vertical normal stress fields obtained with FreeHyTE and Abaqus are plotted at six time points in Figs. 15 and 16, respectively. Again, the quality of the solutions is very similar at all times. The similarity is preserved for all displacements and stress fields, over the whole duration of the analysis.

In the case of the unbounded medium, the bottom boundary is defined as absorbing. To illustrate its effect, the time-histories of the vertical normal stress in points A and C (Fig. 11) and of the shear stress at point B obtained with the absorbing boundary (solid line) are compared with those obtained with a rigid boundary (dashed line) in Fig. 17. As expected, the presence of the absorbing boundary makes no difference in the vertical normal stress field at the top of the medium (Fig. 17(a)), as it recovers the applied normal forces which are not different for the two media. In point B (Fig. 17(b)), the two solutions are similar until around 0.75 s, when the rebound of the shock wave arrives in the bounded medium case. This causes large oscillations of the solution, which are not recovered in the unbounded medium case, as the shock wave is not reflected back into the analysis domain. The effect of the absorbing boundary is also clearly visible in point C (Fig. 17(c)). Similar solutions are obtained until the arrival of the shock wave, around 0.5 s. As the shock wave is not reflected, its duplication in intensity, typical to rigid boundary rebounds, does not occur, so the stresses peak at much lower amplitudes. Around 0.75 s, another peak in the unbounded solution is related to the arrival of a (slower) shear wave, after which the stress amplitude always remains low.

Finally, to illustrate the lack of spurious reflections from the absorbing boundary, the vertical normal stress field in the unbounded medium is plotted at six selected time points in Fig. 18. No spurious reflection is visible from the absorbing boundary, either in terms of normal stress or any other solution field.
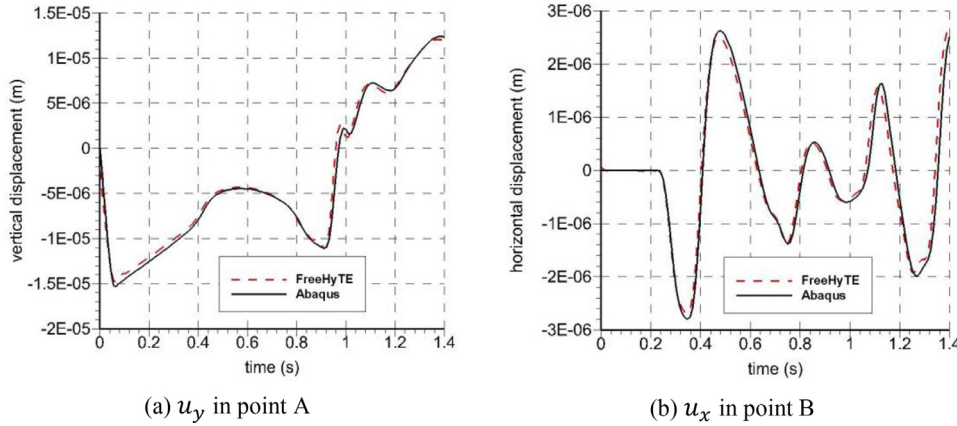
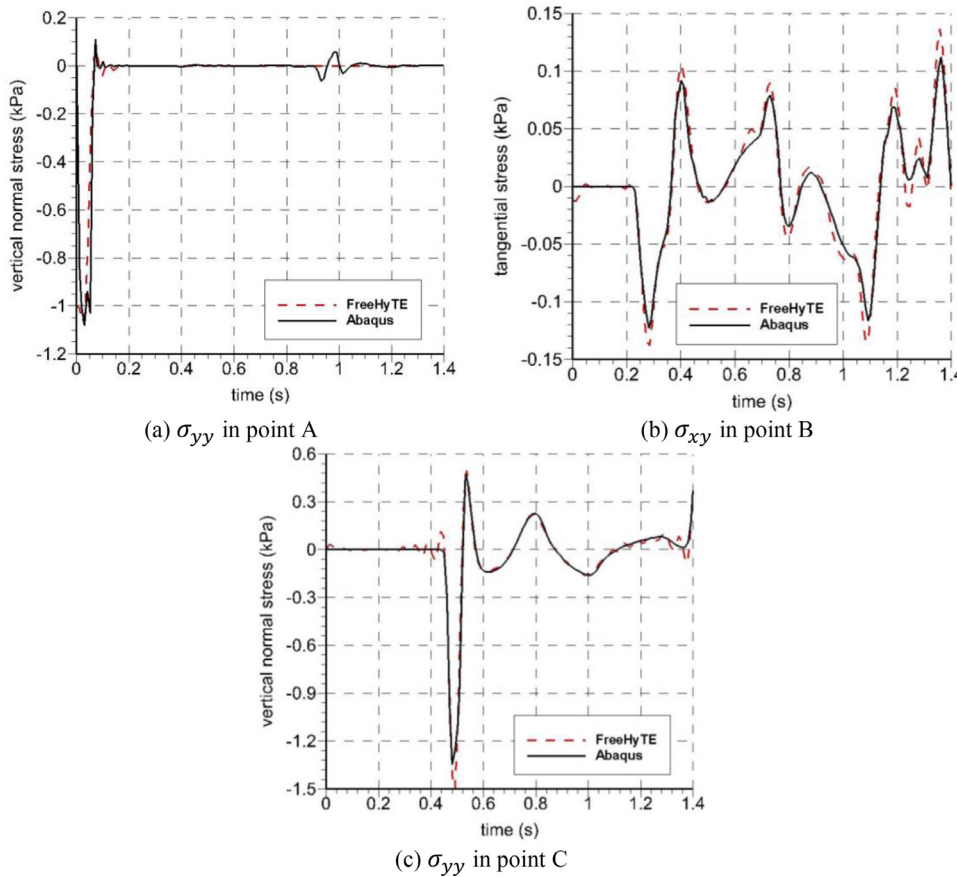**Fig. 12.** Time-history of displacements in selected points.

(a) u_y in point A

(b) u_x in point B

Fig. 13. Time-history of stresses in selected points.

(a) σ_{yy} in point A

(b) σ_{xy} in point B

(c) σ_{yy} in point C

4.2. Shock wave propagation in a semi-infinite saturated medium

The second numerical application is a Heaviside pulse perturbation test on a saturated porous medium. The results are compared with a similar simulation reported by Akiyoshi et al. [1]. The physical model is presented in Fig. 19. The medium is subjected to a vertical excitation $f(x, t) = \bar{f} \cdot \Pi(t)$, applied on a $2L_0 = 8$ m strip and acting exclusively on the solid phase, with $\bar{f} = 1$ kPa and the Heaviside time function $\Pi(t)$ defined by

$$\Pi(t) = \begin{cases} 1.0 \ for \ 0.00 \le t \le 0.01 \\ 0.0 \ for \ t > 0.01 \end{cases} \tag{89}$$

Boundary conditions are applied on the half-structure presented in Fig. 20 as a result of symmetry. The horizontal boundary at $y = 0$ is defined as Neumann, and the vertical boundary at $x = 0$ is Dirichlet. The semi-infinite domain is cropped at $R = 20$ m by an absorbing boundary. The load $f(x, t)$ is applied on the first $L_0 = 4$ m of the Neumann boundary. The tangential stress in the solid phase and the pore pressure are null in that region. On the rest of the Neumann boundary, the normal and tangential stresses and the pore pressure are null. On the Dirichlet boundary at $x = 0$ the normal displacement, the fluid seepage and the tangential stress are null. The domain is discretized using the mesh shown in Fig. 20. The mesh consists of 549 finite elements, with Trefftz bases of order 7. On the essential boundaries, the Chebyshev basis is built on polynomials of degree 4. The mesh is locally refined in the region where the shock load is applied, to account for the large gradients and highly oscillatory nature of the solution in this region. The model has a total of 37,015 degrees of freedom (i.e. the total dimension of the
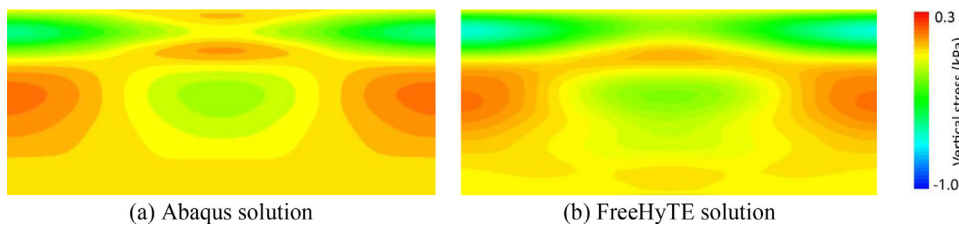
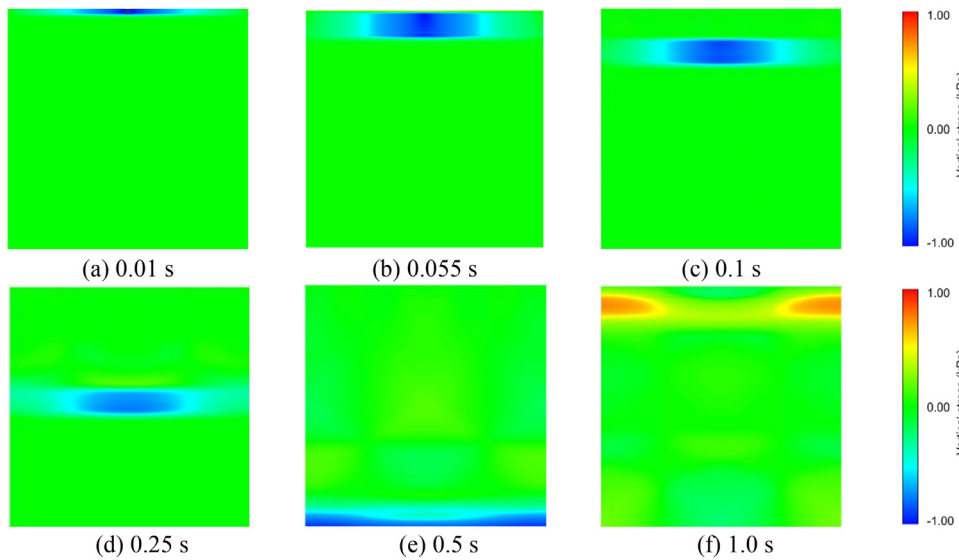**Fig. 14.** Detail of the vertical stress field at $t = 0.95$ s.

(a) Abaqus solution

(b) FreeHyTE solution

Fig. 15. Vertical stress field recovered by Abaqus at selected instants.

(a) 0.01 s

(b) 0.055 s

(c) 0.1 s

(d) 0.25 s

(e) 0.5 s

(f) 1.0 s
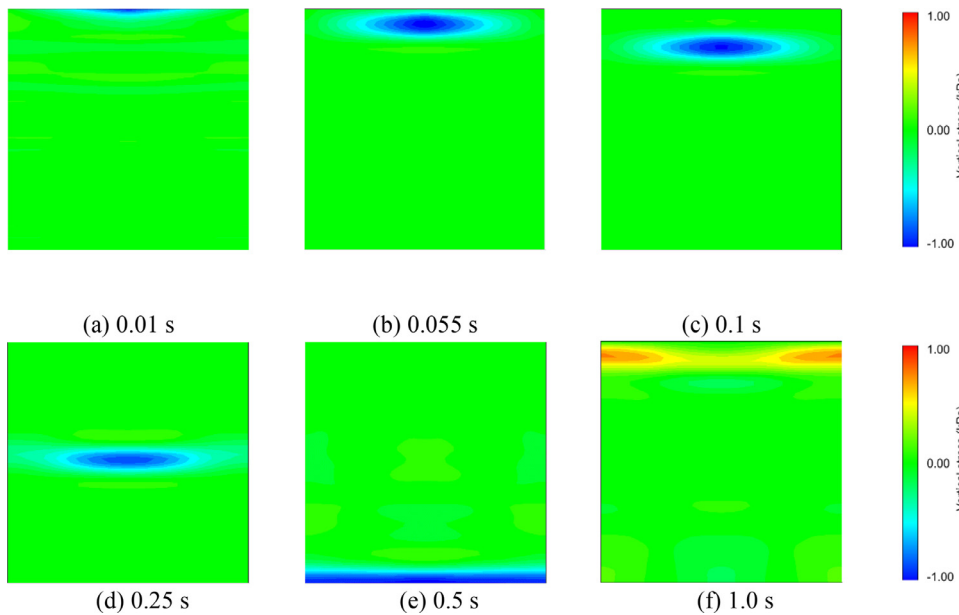
Fig. 16. Vertical stress field recovered by Free-HyTE at selected instants.

(a) 0.01 s

(b) 0.055 s

(c) 0.1 s

(d) 0.25 s

(e) 0.5 s

(f) 1.0 s

solving system (73)). The geomechanical characteristics of the saturated soil are given in Table 2. They were taken from the work of Akiyoshi et al. [1], whose results are used here to validate the results obtained using FreeHyTE.

The total simulation time is $T = 0.5$ s. The time discretization is similar to that used in Section 4.1.

The time-history of the vertical displacement in the solid phase at point $A = (2, -2)$ (Fig. 20) is shown in Fig. 21 and compared with the corresponding results reported in Akiyoshi et al. [1]. The initial silence period of about 0.05 s, taken by the main wavefront to reach

Table 2
Geomechanical properties of the saturated soil.

Fluid density ρ_w (kg/m³)	1000
Mixture density ρ (kg/m³)	2000
Biot's modulus M (Pa)	$3.33 \cdot 10^6$
Young modulus of the solid skeleton E (Pa)	$3.00 \cdot 10^5$
Biot's coefficient α	1.0
Fluid volume fraction n^w	0.3
Poisson's coefficient ν	0.2
Scalar tortuosity a	1.0
Hydraulic conductivity k (m/s)	$9.81 \cdot 10^{-3}$

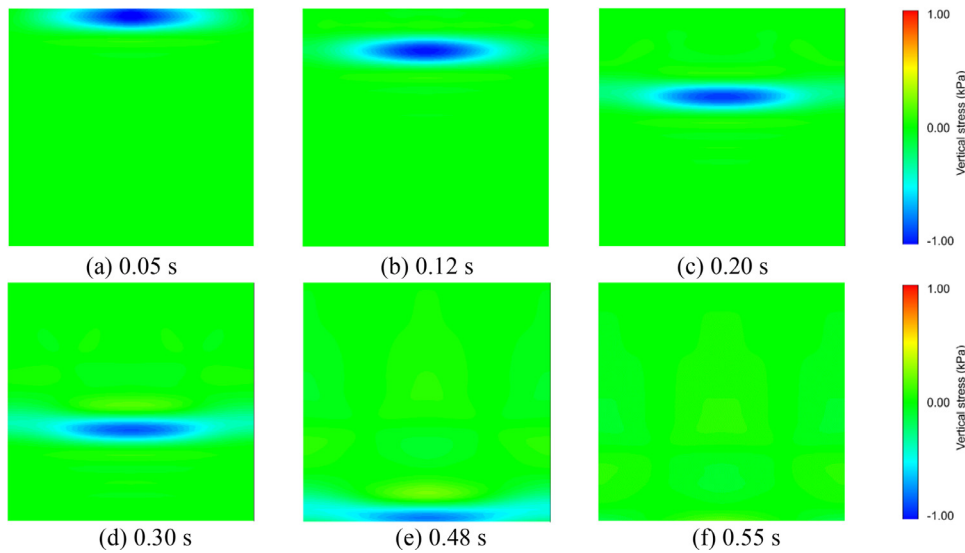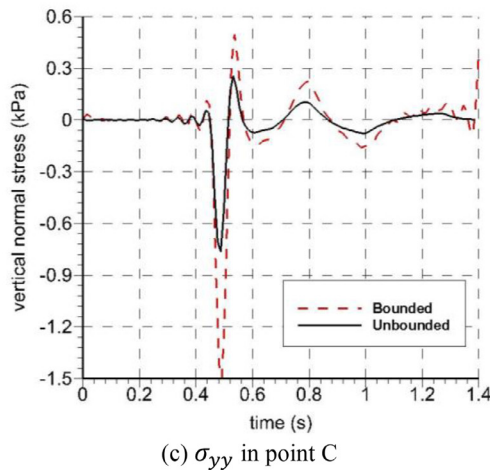**Fig. 17.** Time-history of stresses in selected points.

(a) σ_{yy} in point A

(b) σ_{xy} in point B

(c) σ_{yy} in point C
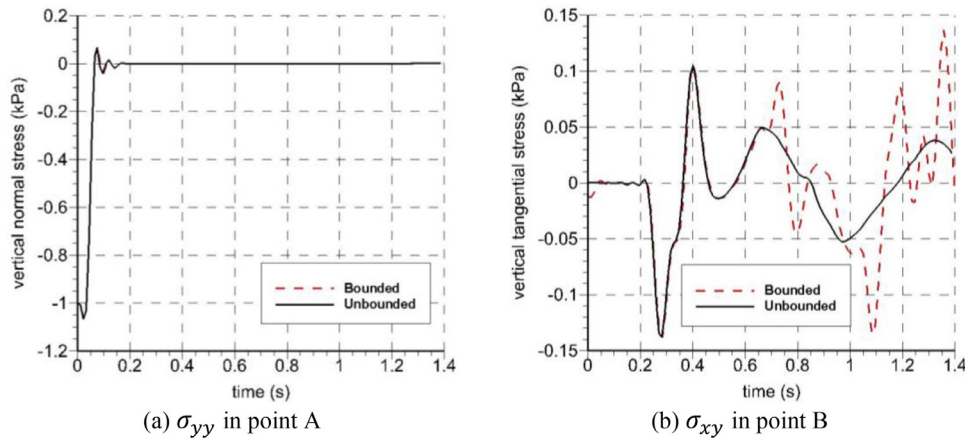
Fig. 18. Vertical stress field in the unbounded medium at selected instants.

(a) 0.05 s (b) 0.12 s (c) 0.20 s

(d) 0.30 s (e) 0.48 s (f) 0.55 s

the depth of point A, is recovered by FreeHyTE and is coherent with Akiyoshi's predictions. The vertical displacement suddenly increases when the shock wave arrives to point A and then stabilizes. This behavior, and indeed the displacement values are in good agreement with the results reported in Akiyoshi et al. [1]. Some spurious higher frequency oscillations seem to be present in the model of Akiyoshi, but are avoided in the FreeHyTE results. It is noted that Akiyoshi republished these results in another paper [2], four years after the first

one, with no spurious oscillations that time. However, the scale of the vertical displacement plot in the more recent paper rendered the exact reading of the plotting points impossible, motivating the comparison with the results reported in the older paper. Moreover, there is a different tendency of the vertical displacement after 0.35 s where FreeHyTE predicts a positive displacement increment, not predicted by Akiyoshi's simulation. Overall, however, the two simulations are in good agreement.
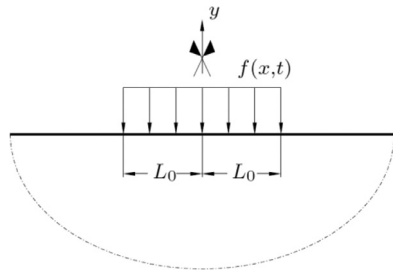
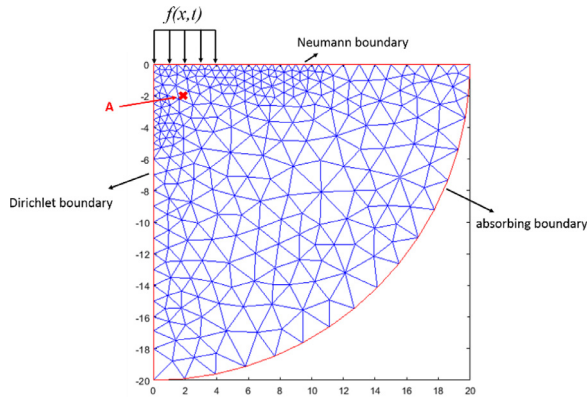Fig. 19. Physical model of the simulation of a shock wave in a biphasic medium.

Fig. 21. Vertical displacement time history at point A (2,−2).

Fig. 20. Boundary conditions and mesh.

4.3. Shock wave propagation in a semi-infinite unsaturated medium

The third numerical application is a shock wave propagation in an unsaturated porous medium. The physical model is similar to that presented in Fig. 19. The medium is subjected to a vertical Heaviside excitation $f(x,t) = \bar{f} \cdot \Pi(t)$ acting on a $2L_0 = 16$ m strip, with $\bar{f} = 1$ kPa and the pulse load $\Pi(t)$ applied during 0.3 s. The total duration of the analysis is $T = 10$ s.

The boundary conditions are applied to the half-structure presented in Fig. 5 and are the same as in Fig. 20. The load $f(x, t)$ in this case, however, is applied on a longer support, $L_0 = 8$ m. The finite element mesh used for the analysis is also shown in Fig. 5. It consists of 300 finite elements, with Trefftz bases of order 9. On the essential boundaries, the traction basis is built on Chebyshev polynomials of degree 3. The model has a total of 30,048 degrees of freedom (i.e. the total dimension of the solving system (73)). The geomechanical characteristics of the unsaturated soil are taken from reference Cao [5] and listed in Table 3.

A fourth family Daubechies wavelet basis is used, with a refinement of 6 generating $2^6 = 64$ spectral problems in space (out of which 32 need to be solved). The number of dyadic points is $2^7 + 1 = 129$.

The vertical stress distribution in the domain is captured at six different times and plotted in Fig. 24. The pore pressures in the wetting fluid at the same time points are presented in Fig. 25. It can be observed that the pressure in the wetting fluid is much lower (two orders of magnitude) than the total vertical stress, meaning that most of the stress is transmitted through the solid skeleton. The pore pressure in the non-

The vertical stress distribution in the domain is captured at six different times and plotted in Fig. 22. The pore pressures at the same six time points are presented in Fig. 23. Both fields recover correctly the enforced boundary conditions and are smooth and continuous between adjacent elements (no stress averaging is used in the plots). It is noted that the stress continuity between adjacent elements is not explicitly enforced in the model, making it a good convergence indicator. The absorbing boundary absorbs the propagated pulse when it reaches the limit of the domain. No spurious reflection is visually detectable.
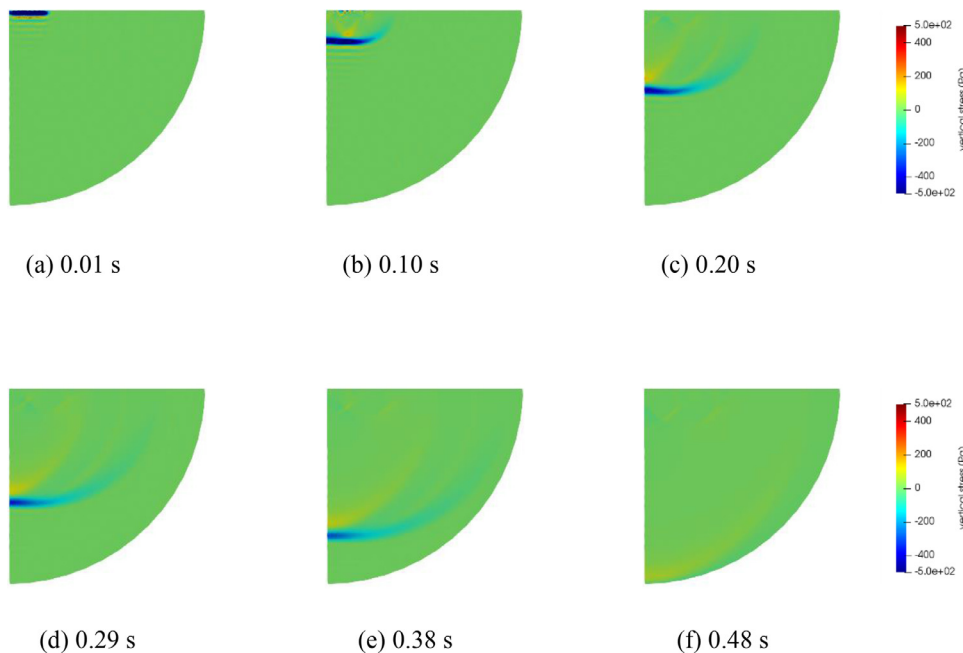

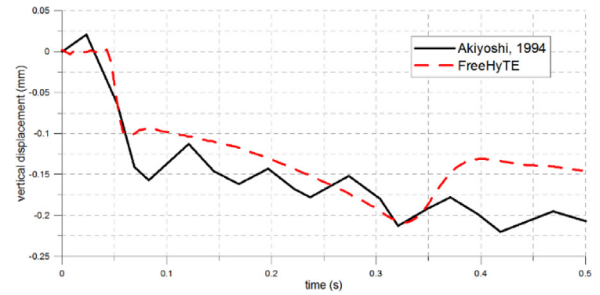Fig. 22. Vertical stress field at different instants.

(a) 0.01 s   (b) 0.10 s   (c) 0.20 s

(d) 0.29 s   (e) 0.38 s   (f) 0.48 s

Fig. 23. Pore pressure field at different instants.

| (a) 0.01 s | (b) 0.10 s | (c) 0.20 s |
| (d) 0.29 s | (e) 0.38 s | (f) 0.48 s |

Fig. 24. Vertical stress field at different instants.
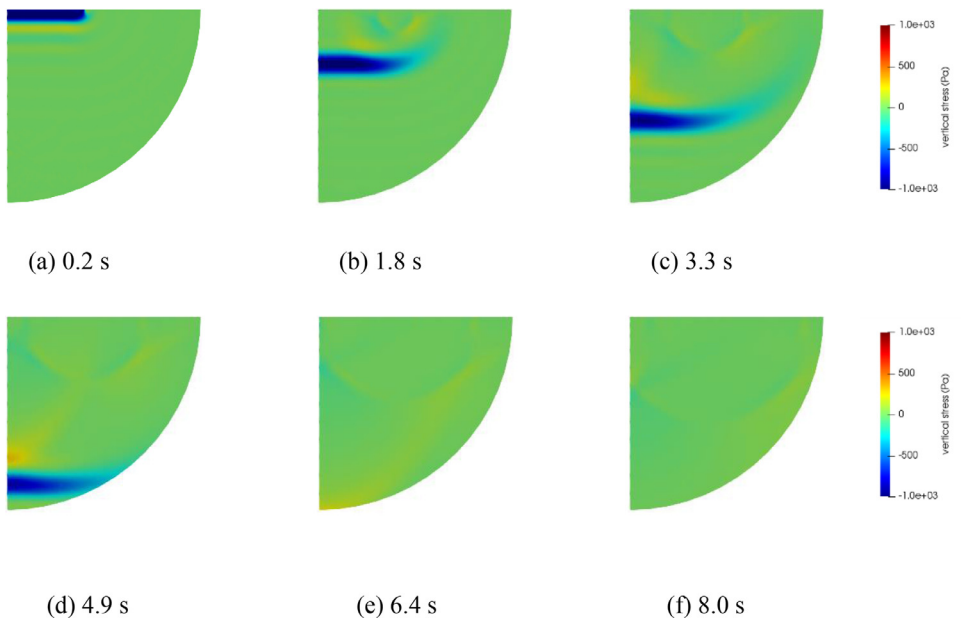
| (a) 0.2 s | (b) 1.8 s | (c) 3.3 s |
| (d) 4.9 s | (e) 6.4 s | (f) 8.0 s |

Table 3
Geomechanical properties for the unsaturated soil.

Bulk modulus of the solid grain K_S (Pa)	$1.00 \cdot 10^5$
Bulk modulus of the wetting fluid K_W (Pa)	$1.00 \cdot 10^4$
Bulk modulus of the non-wetting fluid K_N (Pa)	10
First Lamé coefficient μ^S (Pa)	$1.30 \cdot 10^4$
Second Lamé coefficient λ^S (Pa)	$9.13 \cdot 10^4$
Elastic constant λ^S_{pe} (Pa)	$2.86 \cdot 10^4$
Elastic constant Θ^W (Pa)	$6.85 \cdot 10^4$
Elastic constant Θ^N (Pa)	$1.67 \cdot 10^5$
Degree of saturation S_r	0.8
Intrinsic permeability k_I (m^2)	$1.55 \cdot 10^{-8}$
Density of the solid grain ρ_S (kg/m³)	2000
Density of the wetting fluid ρ_W (kg/m³)	1000
Density of the non-wetting fluid ρ_N (kg/m³)	1.1
Dynamic viscosity of the wetting fluid v^W (Pa·s)	$1.00 \cdot 10^{-3}$
Dynamic viscosity of the non-wetting fluid v^N (Pa·s)	$1.80 \cdot 10^{-5}$
Relative permeability of the wetting fluid k_r^W	0.431
Relative permeability of the non-wetting fluid k_r^N	0.011
Porosity n	0.23

wetting fluid is not represented here because it is too small. Both fields recover correctly the enforced boundary conditions and are smooth and continuous between adjacent elements (no stress averaging is used in the plots). It is noted (as in the previous examples) that the stress continuity between adjacent elements is not explicitly enforced in the model. The absorbing boundary absorbs the propagated pulse when it reaches the limit of the domain and no spurious reflection is visually detectable.

5. Conclusions

Hybrid-Trefftz finite elements are efficient to mitigate the modeling difficulties faced by conventional finite elements in elastodynamic problems. They use approximation bases tailored specifically for the problem that is being solved, with a high content of built-in physical information. This feature accounts for the robustness of the hybrid-Trefftz elements to gross mesh distortion, large solution gradients and extremely small wavelengths. Such issues are typical to highly transient excitations in porous materials, where secondary compression waves travel-
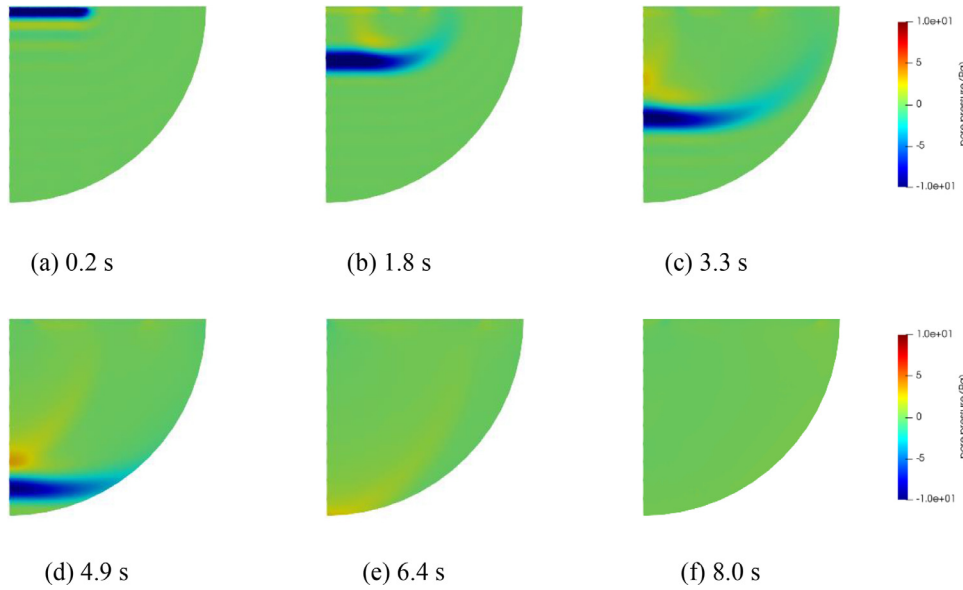
(a) 0.2 s   (b) 1.8 s   (c) 3.3 s

(d) 4.9 s   (e) 6.4 s   (f) 8.0 s

Fig. 25. Pore pressure field in the wetting fluid at different instants.

ling through the fluid(s) have wavelengths that are often a few orders of magnitude shorter than those travelling through the solid skeleton.

The advantages of the hybrid-Trefftz elements are brought to the fingertips of the scientific community through their implementation in the FreeHyTE environment. The resulting modules, for solid, saturated and unsaturated media, enjoy an open-source distribution, user-friendly interfaces, and are supported by a wide range of manuals to get new users and developers acquainted. The documentation, codes and installation kits can be downloaded from the [7].

To the best of the authors' knowledge, this is the first time hybrid-Trefftz elements for dynamic problems defined on solid and porous media are implemented in a public software.

The results obtained with the new modules are successfully validated against commercial software that employs conventional finite elements and against similar results reported in the literature, where available. The absorbing boundary conditions are also shown to efficiently mitigate the spurious vibrations of the inbound waves.

Declaration of Competing Interest

None.

Acknowledgments

Appendix A. Matrices and coefficients for single-phase media

For single phase media, matrix ρ is simply a diagonal matrix having the mass density of the material ρ for its diagonal elements. The operator $\mathcal{D}$ in Eq (26) is

$$\mathcal{D} = \begin{pmatrix} \frac{\partial}{\partial x} & 0 & \frac{\partial}{\partial y} \\ 0 & \frac{\partial}{\partial y} & \frac{\partial}{\partial x} \end{pmatrix} = \left(\mathcal{D}^* \right)^T \tag{90}$$

and the stiffness matrix is,

$$\mathbf{k} = \begin{pmatrix} k_{11} & k_{12} & 0 \\ k_{12} & k_{11} & 0 \\ 0 & 0 & k_{33} \end{pmatrix} \tag{91}$$

The stiffness coefficients are defined as,

$$k_{11} = k_{12} + 2k_{33} \tag{92}$$

where

$$k_{12} = \frac{\lambda\,(1-2\nu)}{1-\nu} \tag{93}$$

for plane stress problems,

$$k_{12} = \lambda \tag{94}$$

for plane strain problems, and

$$k_{33} = \mu \tag{95}$$

for both problems. In definitions (93) to (95), λ and μ are the Lamé's constants and ν is the Poisson's coefficient.

Appendix B. Matrices and coefficients for biphasic media

For biphasic media, matrices ρ_0 and d_0 are,

$$\boldsymbol{\rho_0} = \begin{pmatrix} \rho & 0 & \rho_w & 0 \\ 0 & \rho & 0 & \rho_w \\ \rho_w & 0 & \frac{\rho_w a}{n^w} & 0 \\ 0 & \rho_w & 0 & \frac{\rho_w a}{n^w} \end{pmatrix} \tag{96}$$

$$\boldsymbol{d_0} = \begin{pmatrix} 0 & 0 & 0 & 0 \\ 0 & 0 & 0 & 0 \\ 0 & 0 & \frac{\xi}{n^{w2}} & 0 \\ 0 & 0 & 0 & \frac{\xi}{n^{w2}} \end{pmatrix} \tag{97}$$

and the generalized mass matrix ρ is expressed as,

$$\boldsymbol{\rho} = \begin{pmatrix} \rho & 0 & \rho_w & 0 \\ 0 & \rho & 0 & \rho_w \\ \rho_w & 0 & \rho_{w2} & 0 \\ 0 & \rho_w & 0 & \rho_{w2} \end{pmatrix} \tag{98}$$

where ρ is the mass density of the mixture, ρ_w is the mass density of the liquid phase, and

$$\rho_{w2} = \frac{\rho_w a}{n^w} - \frac{i\,\xi}{\omega n^{w2}} \tag{99}$$

where ξ is the dissipation, n^w is the volume fraction and a is the tortuosity correction factor. The operator D in Eq (26) is

$$D = \begin{pmatrix} \frac{\partial}{\partial x} & 0 & \frac{\partial}{\partial y} & 0 \\ 0 & \frac{\partial}{\partial y} & \frac{\partial}{\partial x} & 0 \\ 0 & 0 & 0 & \frac{\partial}{\partial x} \\ 0 & 0 & 0 & \frac{\partial}{\partial y} \end{pmatrix} = \left(D^*\right)^T \tag{100}$$

and the stiffness matrix is,

$$k = \begin{pmatrix} k_{11} & k_{12} & 0 & k_{14} \\ k_{12} & k_{11} & 0 & k_{14} \\ 0 & 0 & k_{33} & 0 \\ k_{14} & k_{14} & 0 & k_{44} \end{pmatrix} \tag{101}$$

The stiffness coefficients are defined as,

$$k_{11} = k_{12} + 2k_{33} \tag{102}$$

$$k_{12} = \lambda + \alpha^2 M \tag{103}$$

$$k_{33} = \mu \tag{104}$$

$$k_{14} = \alpha M \tag{105}$$

$$k_{44} = M \tag{106}$$

where α and M are the Biot's coefficients [3].

Appendix C. Matrices and coefficients for triphasic media

The expression of the mass ρ_0 and damping d_0 and matrices present in equilibrium Eq (1) are

$$\rho_0 = \begin{pmatrix} n^S \rho^S & 0 & 0 & 0 & 0 & 0 \\ 0 & n^S \rho^S & 0 & 0 & 0 & 0 \\ 0 & 0 & n^W \rho^W & 0 & 0 & 0 \\ 0 & 0 & 0 & n^W \rho^W & 0 & 0 \\ 0 & 0 & 0 & 0 & n^N \rho^N & 0 \\ 0 & 0 & 0 & 0 & 0 & n^N \rho^N \end{pmatrix} \tag{107}$$

$$d_0 = \begin{pmatrix} \mu^W + \mu^N & 0 & -\mu^W & 0 & -\mu^N & 0 \\ 0 & \mu^W + \mu^N & 0 & -\mu^W & 0 & -\mu^N \\ -\mu^W & 0 & \mu^W & 0 & 0 & 0 \\ 0 & -\mu^W & 0 & \mu^W & 0 & 0 \\ -\mu^N & 0 & 0 & 0 & \mu^N & 0 \\ 0 & -\mu^N & 0 & 0 & 0 & \mu^N \end{pmatrix} \tag{108}$$

where n^i, $i = \{S, W, N\}$, represent the volume fractions of each phase, ρ^i are the densities of the solid grain, wetting and non-wetting fluids, and

$$\mu^f = \frac{\left(n^f\right)^2 v^f}{k_I k_r^f} \tag{109}$$

where $f = \{W, N\}$, v^f is the dynamic viscosity of the f-fluid, k_I is the intrinsic permeability and k_r^f is the relative permeability of the f-fluid. The generalized mass matrix ρ is expressed as

$$\rho = \begin{pmatrix} \rho_{SS} & 0 & \rho_{SW} & 0 & \rho_{SN} & 0 \\ 0 & \rho_{SS} & 0 & \rho_{SW} & 0 & \rho_{SN} \\ \rho_{SW} & 0 & \rho_{WW} & 0 & 0 & 0 \\ 0 & \rho_{SW} & 0 & \rho_{WW} & 0 & 0 \\ \rho_{SN} & 0 & 0 & 0 & \rho_{NN} & 0 \\ 0 & \rho_{SN} & 0 & 0 & 0 & \rho_{NN} \end{pmatrix} \tag{110}$$

where,

$$\rho_{SS} = n^S \rho^S - \frac{i}{\omega}\left(\mu^W + \mu^N\right) \tag{111}$$

$$\rho_{SW} = \frac{i}{\omega}\mu^W \tag{112}$$

$$\rho_{SN} = \frac{i}{\omega}\mu^N \tag{113}$$

$$\rho_{WW} = n^W \rho^W - \frac{i}{\omega}\mu^W \tag{114}$$

$$\rho_{NN} = n^N \rho^N - \frac{i}{\omega}\mu^N \tag{115}$$

The operator D is

$$D = \begin{pmatrix} \frac{\partial}{\partial x} & 0 & \frac{\partial}{\partial y} & 0 & 0 \\ 0 & \frac{\partial}{\partial y} & \frac{\partial}{\partial x} & 0 & 0 \\ 0 & 0 & 0 & \frac{\partial}{\partial x} & 0 \\ 0 & 0 & 0 & \frac{\partial}{\partial y} & 0 \\ 0 & 0 & 0 & 0 & \frac{\partial}{\partial x} \\ 0 & 0 & 0 & 0 & \frac{\partial}{\partial y} \end{pmatrix} = \left(D^*\right)^T \tag{116}$$

The stiffness matrix k is,

$$k = \begin{pmatrix} M_{SS} + 2n^S\mu^S & M_{SS} & 0 & M_{SW} & M_{SN} \\ M_{SS} & M_{SS} + 2n^S\mu^S & 0 & M_{SW} & M_{SN} \\ 0 & 0 & n^S\mu^S & 0 & 0 \\ M_{SW} & M_{SW} & 0 & M_{WW} & M_{WN} \\ M_{SN} & M_{SN} & 0 & M_{WN} & M_{NN} \end{pmatrix} \tag{117}$$

where,

$$M_{SS} = n^S\left(K_S + \lambda^S - 2\lambda_{pe}^S\right) - \frac{n^S\left(-2D_N D_W + D_N + D_W\right)\left(K_S - 2\lambda_{pe}^S\right)^2}{K_S\left(1 - D_N D_W\right)} \tag{118}$$

$$M_{SW} = -\frac{\left(1 - D_N\right)D_W K_W n^S\left(\lambda_{pe}^S - K_S\right)}{K_S\left(1 - D_N D_W\right)} \tag{119}$$

$$M_{SN} = -\frac{D_N\left(1 - D_W\right)K_N n^S\left(\lambda_{pe}^S - K_S\right)}{K_S\left(1 - D_N D_W\right)} \tag{120}$$

$$M_{WW} = K_W n^W - \frac{D_W K_W^2 n^S}{K_S\left(1 - D_N D_W\right)} \tag{121}$$

$$M_{WN} = \frac{D_N D_W K_N K_W n^S}{K_S\left(1 - D_N D_W\right)} \tag{122}$$

$$M_{NN} = K_N n^N - \frac{D_N K_N^2 n^S}{K_S\left(1 - D_N D_W\right)} \tag{123}$$

$$D_W = \frac{K_S n^W}{K_S n^W + K_W n^S + n^S\left(n^W\right)^2 \Theta^W} \tag{124}$$

$$D_N = \frac{K_S n^N}{K_S n^N + K_N n^S + n^S\left(n^N\right)^2 \Theta^N} \tag{125}$$

and μ^S and λ^S are the Lamé's coefficients. Elastic constants λ_{pe}^S, Θ^W and Θ^N can be determined experimentally following the procedures described in Wei and Muraleetharan [26] and K_i, $i = \{S, W, N\}$, are the bulk moduli of each phase.

Appendix D. Absorbing boundary flexibility matrices

For single-phase media, the inverse of the absorbing boundary flexibility matrix present in Eq (6) is given by Lysmer and Kuhlemeyer [14] as,

$$C^{-1} = -i \begin{pmatrix} \beta_P (k_{12} + 2k_{33}) & 0 \\ 0 & \beta_S k_{33} \end{pmatrix} \tag{126}$$

The inverse of the absorbing boundary flexibility matrix for biphasic media is given by Moldovan [16] as,

$$C^{-1} = \begin{pmatrix} C_{11} & 0 & C_{13} \\ 0 & C_{22} & 0 \\ C_{31} & 0 & C_{33} \end{pmatrix} \tag{127}$$

$$C_{11} = C \left[\chi \left(\gamma_{P1}^W \beta_{P2} - \gamma_{P2}^W \beta_{P1} \right) + \alpha \gamma_{P1}^W \gamma_{P2}^W \left(\beta_{P2} - \beta_{P1} \right) \right] \tag{128}$$

$$C_{13} = C \left[\chi \left(\beta_{P1} - \beta_{P2} \right) + \alpha \left(\gamma_{P1}^W \beta_{P1} - \gamma_{P2}^W \beta_{P2} \right) \right] \tag{129}$$

$$C_{22} = -i \, \beta_S \mu \tag{130}$$

$$C_{31} = C \left[\alpha \left(\gamma_{P1}^W \beta_{P2} - \gamma_{P2}^W \beta_{P1} \right) + \gamma_{P1}^W \gamma_{P2}^W \left(\beta_{P2} - \beta_{P1} \right) \right] \tag{131}$$

$$C_{33} = C \left[\left(\gamma_{P1}^W \beta_{P1} - \gamma_{P2}^W \beta_{P2} \right) + \alpha \left(\beta_{P1} - \beta_{P2} \right) \right] \tag{132}$$

$$C = -i \, \frac{M}{\gamma_{P1}^W - \gamma_{P2}^W} \tag{133}$$

$$\chi = \alpha^2 + \frac{\lambda + 2\mu}{M} \tag{134}$$

The absorbing boundary flexibility matrix for triphasic media is

$$C = \begin{pmatrix} C_{11} & 0 & C_{13} & C_{14} \\ 0 & C_{22} & 0 & 0 \\ C_{31} & 0 & C_{33} & C_{34} \\ C_{41} & 0 & C_{43} & C_{44} \end{pmatrix} \tag{135}$$

where the coefficients are the solutions of the problem

$$\begin{pmatrix} C_{11} & C_{13} & C_{14} \\ C_{31} & C_{33} & C_{34} \\ C_{41} & C_{43} & C_{44} \end{pmatrix} = i \begin{pmatrix} \beta_{P1}^{-1} & \beta_{P2}^{-1} & \beta_{P3}^{-1} \\ \gamma_{P1}^W \beta_{P1}^{-1} & \gamma_{P2}^W \beta_{P2}^{-1} & \gamma_{P3}^W \beta_{P3}^{-1} \\ \gamma_{P1}^N \beta_{P1}^{-1} & \gamma_{P2}^N \beta_{P2}^{-1} & \gamma_{P3}^N \beta_{P3}^{-1} \end{pmatrix}$$
$$\cdot \begin{pmatrix} C_{s11} & C_{s12} & C_{s13} \\ C_{s21} & C_{s22} & C_{s23} \\ C_{s31} & C_{s32} & C_{s33} \end{pmatrix}^{-1} \tag{136}$$

$$C_{s11} = M_{SS} + 2n^S \mu^S + \gamma_{P1}^W M_{SW} + \gamma_{P1}^N M_{SN} \tag{137}$$

$$C_{s12} = M_{SS} + 2n^S \mu^S + \gamma_{P2}^W M_{SW} + \gamma_{P2}^N M_{SN} \tag{138}$$

$$C_{s13} = M_{SS} + 2n^S \mu^S + \gamma_{P3}^W M_{SW} + \gamma_{P3}^N M_{SN} \tag{139}$$

$$C_{s21} = M_{SW} + \gamma_{P1}^W M_{WW} + \gamma_{P1}^N M_{WN} \tag{140}$$

$$C_{s22} = M_{SW} + \gamma_{P2}^W M_{WW} + \gamma_{P2}^N M_{WN} \tag{141}$$

$$C_{s23} = M_{SW} + \gamma_{P3}^W M_{WW} + \gamma_{P3}^N M_{WN} \tag{142}$$

$$C_{s31} = M_{SN} + \gamma_{P1}^W M_{WN} + \gamma_{P1}^N M_{NN} \tag{143}$$

$$C_{s32} = M_{SN} + \gamma_{P2}^W M_{WN} + \gamma_{P2}^N M_{NN} \tag{144}$$

$$C_{s33} = M_{SN} + \gamma_{P3}^W M_{WN} + \gamma_{P3}^N M_{NN} \tag{145}$$

and

$$C_{22} = i \, \left(\beta_S \, n^S \mu^S \right)^{-1} \tag{146}$$

References

[1] Akiyoshi T, Fuchida K, Fang HL. Absorbing boundary conditions for dynamic analysis and fluid-saturated porous media. Soil Dyn Earthq Eng 1994;13:387–97. https://doi.org/10.1016/0267-7261(94)90009-4.

[2] Akiyoshi T, Sun X, Fuchida K. General absorbing boundary conditions for dynamic analysis of fluid-saturated porous media. Soil Dyn Earthq Eng 1998;17:397–406. https://doi.org/10.1016/S0267-7261(98)00026-8.

[3] Biot MA. Theory of propagation of elastic waves in a fluid saturated porous solid. II. Higher frequency range. J Acoust Soc America 1956;28(2):179–91. https://doi.org/10.1121/1.1908239.

[4] Brooks H, Corey AT. Hydraulic properties of porous media. Fort Collins: Hydrology Paper No 3, Colorado State University; 1964.

[5] Cao DT. Hybrid-Trefftz finite elements for elastostatic and elastodynamic problems in porous media, Portugal: Universidade Católica Portuguesa; 2013. PhD Thesis.

[6] Daubechies I. Orthonormal bases of compactly supported wavelets. Comm Pure Appl Math 1988;41:909–96.

[7] FreeHyTE Release Page, https://www.sites.google.com/site/ionutdmoldovan/freehyte; 2016 [accessed 01.11.2019].

[8] Freitas JAT. Mixed finite element solution of time-dependent problems. Comput Method Appl M Eng 2008;197:3657–78. https://doi.org/10.1016/j.cma.2008.02.014.

[9] Freitas JAT, Moldovan ID, Cismaşiu C. Hybrid-Trefftz displacement element for bounded and unbounded poroelastic media. Comp Mech 2011;48:659–73. https://doi.org/10.1007/s00466-011-0612-7.

[10] Hartmann J, Heubrandtner T, Kunter K, Pippan R, Fellner B, Martinez JD. A special purpose Trefftz-element for mode III crack tip loading. Eng Fract Mech 2018;192:210–24. https://doi.org/10.1016/j.engfracmech.2018.01.030.

[11] Herrera I. Boundary methods. An algebraic theory. Boston, London, Melbourne: Pitman Advanced Publishing Program; 1984.

[12] Horák M, Patzák B, Novák J. An isogeometric extension of Trefftz method for elastostatics in two dimensions. Int J Numer Methods Eng 2018;114(11):1213–27. https://doi.org/10.1002/nme.5783.

[13] Jirousek J. Basis for development of large finite elements locally satisfying all field equations. Comput Method Appl M 1978;14:65–92. https://doi.org/10.1016/0045-7825(78)90013-0.

[14] Lysmer J, Kuhlemeyer RL. Finite dynamic model for infinite media. J Eng Mech Division, Proc ASCE 1969;95:859–77.

[15] Martins PHC, Bussamra FLS, Lucena Neto E. Three dimensional hybrid-Trefftz stress finite elements for plates and shells. Int J Num Method Eng 2018;113(11):1676–96. https://doi.org/10.1002/nme.5715.

[16] Moldovan ID. Hybrid-Trefftz finite elements for elastodynamic analysis of saturated porous media, Portugal: Universidade Técnica de Lisboa; 2008. PhD Thesis.

[17] Moldovan ID. A new particular solution strategy for hyperbolic boundary value problems using hybrid-Trefftz displacement elements. Int J Num Method Eng 2015;102(6):1293–315. https://doi.org/10.1002/nme.4836.

[18] Moldovan ID, Cao DT, Freitas JAT. Hybrid-Trefftz displacement finite elements for elastic unsaturated soils. Int J Comp Method, Special Issue on Computational Geomechanics 2014;11(2). https://doi.org/10.1142/S021987621342005X.

[19] Moldovan ID, Cismaşiu I. FreeHyTE: a hybrid-Trefftz finite element platform. Adv Eng Softw 2018;121:98–119. https://doi.org/10.1016/j.advengsoft.2018.03.014.

[20] Moldovan ID, Freitas JAT. Hybrid-Trefftz displacement and stress elements for bounded poroelasticity problems. Comp Geo 2012;42:129–44. https://doi.org/10.1016/j.compgeo.2011.12.003.

[21] Piltner R. Special finite elements with holes and internal cracks. Int J Numer Methods Eng 1985;21:1471–85. https://doi.org/10.1002/nme.1620210809.

[22] Qin QH. Postbuckling analysis of thin plates by a hybrid Trefftz finite element method. Comput Method Appl M 1995;128:123–36. https://doi.org/10.1016/0045-7825(95)00873-5.

[23] Sato D, Hasegawa K, Mizukami N, Tsushima Y. Hybrid Trefftz finite-element method for analyzing the eigenmodes of optical fibers. J Lightwave Technol 2019;37:1029–36. https://doi.org/10.1109/JLT.2018.2885311.

[24] Tong P, Pian PH, Lasry SL. A hybrid-element approach to crack problems in plane elasticity. Int J Numer Methods Eng 1973;7:297–308. https://doi.org/10.1002/nme.1620070307.

[25] Trefftz E. Ein Gegenstück zum ritzschen verfahren. In: Proceedings of the 2nd International Congress of Applied Mechanics; 1926. p. 131–7.

[26] Wei C, Muraleetharan KK. A continuum theory of porous media saturated by multiple immiscible fluids: I. linear poroelasticity. Int J Eng Sci 2002;40:1807–33. https://doi.org/10.1016/S0020-7225(02)00068-X.